This is a preprint of the following article:

Y. Lyu, A. Seth, and R. P. Liem. Fuel consumption and trailing-edge noise tradeoff studies via mission-based airfoil shape optimization. Aerospace Science and Technology, 2024. 10.1016/j.ast.2024.109331.

The published article may differ from this preprint, and is available at the DOI above.

Fuel consumption and trailing-edge noise tradeoff studies via mission-based airfoil shape optimization

Yuan Lyu* Arjit Seth† Rhea Liem‡

The Hong Kong University of Science and Technology (HKUST), Hong Kong SAR

Abstract Aerodynamic drag is often used as a proxy for fuel consumption in aircraft design. However, the aeroacoustic byproduct of airfoil design, such as trailing-edge noise (TEN), is yet to be considered in aircraft applications, despite its inclusion in wind turbine designs. To explore the impact of TEN in airfoil design for aircraft, we establish a mission-based aerodynamic shape optimization framework. A surrogate-based detailed flight mission analysis (that can simulate a flight mission from takeoff to landing) is incorporated into the optimization framework to obtain realistic flight conditions along the takeoff and landing—which are important to assess TEN metrics—and calculate accurate fuel consumption, where both are used to evaluate the objective function. To assess its effectiveness, we compare the results against those of the conventional single-point optimization. Not surprisingly, the mission-based optimization simultaneously reduces fuel consumption and TEN, while the single-point optima (performed at the low Mach region) reduce TEN at the expense of higher fuel consumption. This is due to the tradeoff between aerodynamic performance in the transonic region and aeroacoustic performance in the low Mach region, which cannot be properly analyzed without including flight mission analysis in the optimization loop.

1 Introduction

Environmental impact consideration has gained importance in the development of aircraft technology and operations, owing to the increased aviation-related emissions in recent years. In 2019, the total CO_2 emissions from commercial aviation were 918 million metric tons, which accounted for 1.3% of global greenhouse gas emissions [1]. In addition, noise pollution has also been recognized as another adverse environmental impact of aviation [2]. However, simultaneously mitigating these environmental impacts is challenging, due to the inherent tradeoff between fuel consumption and noise. As an example, Airbus A340 underwent a redesign of the engine, nacelle, pylon, and wing

*Postdoctoral Fellow, Department of Mechanical and Aerospace Engineering.

†Research Assistant, Department of Mechanical and Aerospace Engineering.

‡Associate Professor, Department of Mechanical and Aerospace Engineering, AIAA Member.

to meet Heathrow Airport's noise requirements; however, the reduction of 1-2 dB trades a 1-2 % increment of fuel burn [3].

Initial attempts have shown that integrating the environmental performance at the aircraft conceptual design stage could help decrease the environmental impact of commercial aviation [4]. However, the simultaneous consideration of fuel consumption and noise emission is less common in aerodynamic shape optimization (ASO), which corresponds to the detailed design stage. A classic ASO formulation determines the airfoil or wing geometry of an aircraft that minimizes aerodynamic drag at a given Mach number, which can consequently affect the fuel economy [5]. To a certain extent, the resulting aerodynamic flow contributes to the aircraft's source noise, such as the trailing-edge noise (TEN), albeit not the major contributor to the overall aircraft noise. While TEN has been considered in the airfoil design for wind turbines [6], its consideration in aircraft design is still scarce.

In general, aircraft noise is mainly caused by turbulent flows through the propulsive system (engine), as well as the non-propulsive system (airframe), especially high-lift devices and landing gears [7]. Indeed, TEN only constitutes a minor component in comparison with other major airframe noise sources. However, considering the ambitious targets for fuel efficiency and noise reduction [8, 9], gaining further noise reduction cannot rely solely on the major components, which have already demonstrated considerable advancements. Having said that, the contribution from other minor components, such as TEN, cannot be overlooked and should be considered when optimizing airfoil shape design. In this work, we aim to investigate the impact and tradeoffs of considering TEN in airfoil design for aircraft design applications, in addition to the fuel efficiency consideration.

Although most ASO formulations have not considered fuel consumption and source noise simultaneously, previous studies have demonstrated tradeoffs between aerodynamic and aeroacoustic performance. As an example, Hosder *et al.* investigated the effect of airfoil and wing geometry and their resultant aerodynamic lift coefficient (C_L) on the TEN metrics [10]. Their findings suggest that reducing the lift coefficient and thickness ratio can lead to a decrease in TEN. This observation indicates that aeroacoustic consideration must be included in the initial design process to minimize its impact on other aerodynamic performance [11]. To date, due to the complexity of analyzing aeroacoustics, most aerodynamic-aeroacoustic optimizations are limited to 2D airfoil shapes [6, 11, 12]. With this consideration and to ensure that we can obtain meaningful insight and results within a practical computational budget, we will also limit our present study to 2D airfoil shape optimization.

In previous research where TEN was factored into ASO, optimizations were frequently conducted under a fixed flow condition. As an example, Jouhaud *et al.* performed a surrogate-based multidisciplinary shape optimization on a 2D NACA subsonic airfoil [12], where the objective function included the far-field radiated TEN noise and aerodynamic forces. In this work, the optimum airfoils were found under a fixed high Reynolds number and low-subsonic flow condition. Such a fixed-condition (i.e., single-point) formulation is also common in airfoil shape optimizations for

wind turbine design applications, with the objective to reduce noise emissions while considering the aerodynamic performance [6]. When applied in the context of aircraft design, this single-point optimization approach could potentially sacrifice performance at other flight conditions. Optimizing the airfoil design at the low Mach region, for instance, might lead to suboptimal performance at the transonic cruise phase and result in higher fuel consumption, which is undesirable. This is particularly relevant when both fuel consumption and TEN are considered at the same time since the corresponding dominant flight conditions are different (low Mach for TEN at low altitude—for community noise consideration—and transonic for fuel consumption). Furthermore, the fuel performance cannot be thoroughly considered in a single-point optimization.

To address these issues, we propose a mission-based optimization framework, where a complete flight mission analysis is performed at each optimization iteration. The mission analysis computes fuel consumption for predefined mission parameters and assesses TEN at different points along the mission profile. As mentioned, the present study is still limited to designing a 2D airfoil, whereas aerodynamic performance values concerning a 3D wing are required in the mission analysis framework. This calls for the conversion from the obtained aerodynamic values of the 2D model to suitable 3D values, which will be performed accordingly. While the resulting geometry might not be truly representative of a realistic aircraft design, the mission-based optimization results presented herein will still offer valuable insights into the tradeoffs between efficient aerodynamics and favorable aeroacoustics in airfoil shape optimization for aircraft, while considering a subset of the complex operational constraints—which is the main aim of this research.

The developed framework will be demonstrated to optimize an airfoil section from a conventional wing configuration. However, the framework will also be applicable to future unconventional configurations (such as supersonic transport aircraft or blended wing body configuration), when relevant data and information are available. To substitute the costly evaluations of aerodynamic, aeroacoustic, and engine performance, surrogate models are utilized in the relevant modules. The framework is developed to be modular and flexible to allow for potential future extensions. The modular architecture of the framework makes using different surrogate models possible and allows for the integration of more sophisticated models in the future, such as the appropriate noise models for high-lift devices.

This paper is organized as follows. We briefly review relevant research on mission-based ASO and aerodynamic noise estimation in Section 2. Section 3 presents the descriptions of the baseline wing geometry and optimization cases considered in this study. Section 4 describes the methodologies required to construct a mission-based optimization framework. Section 5 presents the optimization results and discusses the benefits of performing mission-based optimizations. Finally, the summary and conclusion are presented in Section 6.

2 Background

In this section, we provide a review of the existing literature on ASO and aerodynamic noise estimation.

2.1 ASO formulation: from single-point to mission-based

Early work in ASO only considered a fixed nominal flight condition (typically from the cruise phase of a predefined design mission). The resulting optimal wing/airfoil may suffer a performance degradation at *off-design* conditions, that is, conditions other than the nominal one [13]. Multipoint optimization can alleviate this situation by considering a set of operating conditions [14], i.e., different combinations of Mach number, angle of attack, altitude, and lift coefficient (or aircraft weight) [15]. However, even in multipoint optimization cases, all flight conditions used in these studies are based on the design mission, which cannot completely represent the full spectrum of real flight operations. Further improvement can be achieved by infusing operational data into ASO formulation, typically by performing mission analyses of a set of flights. Initial attempts involved performing the mission analysis *offline*, i.e., outside the optimization loop, to reduce the computational complexity [16]. To further reduce the computational cost, some researchers resolved to use low-fidelity models in the optimization loop, such as a parametric model combined with piecewise analytic model [17] and the Bréguet range equation [18].

The integration of numerical mission analysis into an aircraft design loop has been done at the conceptual design stage for sizing purposes [19]. Nevertheless, its integration with ASO has been shown to be more challenging. Existing attempts rely on using simplified mission profile and analysis [20, 15, 21], which sacrifices accuracy. Among these works, Jasa *et al.* included a mission analysis module in the loop to optimize the mission profile and morphing wing twist [20]. Extending the scope to include the airline operation aspect, Hwang *et al.* presented a simultaneous allocation-mission-design optimization module aimed at maximizing the profit of a next-generation transport aircraft using the modular analysis and unified derivatives architecture [15]. In this work, the authors explicitly mentioned that the focus was on the development of a large-scale optimization framework, and not how realistic the results would be. Lastly, Adler and Martins introduced a mission-based aerostructural optimization through `OpenConcept`[1] [21]. In these works, they used a simple mission profile that excluded detailed takeoff and landing phase models, which would hinder the considerations of flight conditions relevant to community noise assessment. Therefore, these frameworks do not have the required level of detail to achieve our specific objective.

To address this problem, we develop a mission-based ASO approach. In this approach, all flight conditions throughout the mission phases are considered via performing mission analysis in the loop. Upon analyzing the mission for a given set of design variables, the objective functions and constraints are evaluated.

2.2 Aerodynamic noise estimation

Aerodynamic noise generation is inherently connected to local flow characteristics. Therefore, it is important to model the coupling between aerodynamic and acoustic aspects of flow to ensure that the implementation of any noise reduction technique will not degrade the aerodynamic performance, and vice versa. During a flight, an aircraft goes through various flight conditions, and the flow

[1] `https://github.com/mdolab/openconcept` (last accessed on 15 February 2024).

characteristics associated with these flight conditions will affect source noise. This relationship can be modeled in a flight mission analysis procedure. In this work, we focus on incorporating the airfoil's TEN prediction model into the mission analysis procedure, especially in the low-altitude landing and takeoff phases (LTO cycle), which is relevant to community noise assessment.

TEN is generated by the vortical disturbances created along the airfoil surface and scattered over the trailing edge. Its propagation to the far-field can be separated into three physical processes, namely sound generation, propagation, and radiation. Depending on the complexity of the TEN prediction problem, the modeling methods can be categorized into three groups, which are semi-empirical, hybrid, and direct approaches [22]. The semi-empirical method is the simplest and the least expensive one. However, the usability of this type of method, such as the one proposed by Brooks *et al.* [23], is restricted as the model is calibrated solely based on experimental data obtained from the NACA0012 airfoil section. In contrast, the direct methods are more accurate but difficult to achieve because of scale differences between the aerodynamics and aeroacoustic-related phenomena [24]. To balance computational cost and accuracy, hybrid methods have increasingly become more popular and widely used. In general, their efficiency is achieved by decoupling the source flow and aeroacoustic computation.

The calculation of hybrid methods can typically be divided into two parts: an aerodynamic part to calculate the unsteady flow in the source region by computational fluid dynamics (CFD), and an acoustic part, where acoustic propagation methods are used to yield the source wave radiation to the far-field [25]. To further reduce the computational cost, the source turbulent flow problem can be resolved by a Reynolds-averaged Navier-Stokes (RANS) simulation [26]. However, the RANS solution cannot provide unsteady information about the flow. Therefore, stochastic methods are typically used to generate the missing data. For the acoustic part, purely statistical approaches provide the least expensive approach of all the hybrid methods [22], such as the RANS-based Statistical Noise Model [27]. Alongside a model for the turbulent velocity cross-spectrum, the Green's function for a semi-infinite half-plane is commonly used to generate a far-field acoustic auto-spectrum. It is worth noting that most wall-pressure based models are used to predict the far-field acoustic pressure by means of conversion using Amiet's theory [28] or Howe's theory [29]. The applicability of the model is well-established in this setting as researchers have been developing the wall-pressure spectrum (WPS) model for this purpose since the 1950s [30]. With the help of experimental data [26], more models have been proposed to represent wall pressure turbulence fluctuations. Of all the models developed for this purpose, the Rozenberg and Kamruzzaman models have been shown to yield better predictions than any other models for airfoil flows [31].

In this paper, we choose the hybrid method for TEN prediction purposes. In particular, three modules are involved in the model construction, where RANS is selected to model the flow at the source region, Kamruzzaman's model is chosen as the WPS model, and Howe's theory is utilized as the acoustic model. Each of these methods will be further elaborated in Section 4.2.2. The computational efficiency offered by this approach allows for performing design exploration and optimization within a practical computational budget.

3 Problem description

In this section, we describe the baseline wing geometry and the optimization cases—including single-point and mission-based optimizations—considered in this study.

3.1 Wing geometry

As mentioned in Section 1, an airfoil section from a conventional wing configuration is considered in this study. In particular, we use the eta65 airfoil section of the National Aeronautics and Space Administration (NASA) Common Research Model (CRM) wing[2] as the baseline airfoil for the shape optimization problem. This airfoil is the representative shape at the 65% semi-span location of the CRM wing. CRM is selected as it has been commonly used in ASO and aerostructural research [16, 32, 33]. The CRM wing geometry is shown in Fig. 1, where the 65% spanwise location is indicated by the thick black line in the upper figure and the corresponding airfoil cross section is shown in red in the bottom figure. As shown, the CRM wing is a sweptback wing with a sweep angle of 31.5°, calculated at the 50%-chord line (the sweep angle of the leading edge is 35°). The airfoil section that is used in our analyses is taken from an unswept cross-section of the wing, that is, the wing cross-section that is perpendicular to the 50%-chord line. The corresponding conversion of the flow conditions from the 3D wing to the 2D cross section (for aerodynamic performance evaluation purposes) will be described in Section 4.4.

3.2 Airfoil shape optimization problems

The ASO problem presented in this paper is posed as a constrained multi-objective optimization problem, in which the airfoil refers to the cross-section of a wing of a passenger jet aircraft. In addition to performing a mission-based optimization, a conventional single-point optimization is also completed for comparison purposes. Each of these optimization formulations is described briefly below. Both optimizations are performed using the non-dominated sorting genetic algorithm II (NSGA-II) algorithm.

3.2.1 Single-point ASO formulation

The single-point optimization is formulated as a lift-constrained drag and TEN minimization problem, which is similar to the work presented by Zhou *et al.* [11]. This formulation is summarized in Table 1. To perform the flow analyses, freestream velocity is set to be 72 m/s, following the work conducted by Zhou *et al.* [34]. It is worth noting that setting the objective to minimize the total flight fuel consumption is not viable in this single-point optimization. Therefore, the drag coefficient (C_D) and A-weighted overall sound pressure level (OASPL) are used as the aerodynamic and aeroacoustic metrics, respectively. The noise metric, A-weighted OASPL, will be further described in Section 4.2.2. The lift coefficient C_L is constrained to $C_L^* = 0.4$.

[2] https://commonresearchmodel.larc.nasa.gov/home-2/high-speed-crm/experimental-approach/model-description/ (last accessed on 15 February 2024).

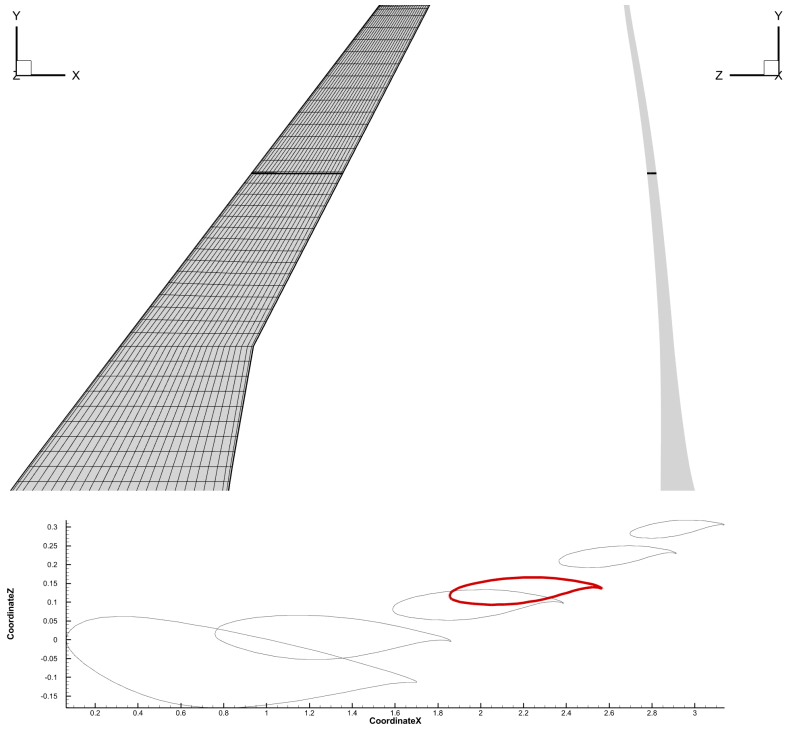


Figure 1: CRM wing and the selected baseline airfoil. (For interpretation of the colors in the figure(s), the reader is referred to the web version of this article.)

3.2.2 Mission-based ASO formulation

In this work, the mission-based ASO is formulated to minimize the total fuel consumption of a flight mission and the maximum TEN generated by the airfoil in the LTO cycle. Note that since the TEN evaluation is only limited to the LTO phase, only the low Mach region ($0.1 \leq M \leq 0.25$) will be considered in the calculation, which will be further described in Section 4.3.2. The design variables are the shape of the airfoil, which will be expressed in terms of a geometric parameterization (to be further described in Section 4.3.1). The mission requirements in terms of payload, range, and other mission and speed parameters are modeled as constraints of the optimization. This mission-based ASO formulation is presented in Table 2, which lists the objective functions, design variables, and constraints of the optimization. The aircraft performance evaluation is mathematically formulated

Table 1: Single-point optimization problem formulation.

	Function/variable	Description
minimize	C_D	Drag coefficient
	OASPL	Airfoil's trailing-edge noise
with respect to	$\mathbf{x}_{\text{shape}}$	Shape variables
subject to	$V = 72$ m/s	Velocity requirement
	$C_L = C_L^*$	Lift requirement

via a flight performance analysis procedure, which will be further described in Section 4.1, and performed by assuming a nominal mission profile.

At each design iteration, the relevant quantities of interest (e.g., lift, drag, fuel consumption, TEN) of the selected airfoil are calculated to evaluate the objective functions and constraints. The aerodynamic value conversion from 2D airfoil to 3D wing, which is required to perform the flight mission analysis, will be presented in Section 4.4.

Table 2: Mission-based optimization problem formulation.

	Function/variable	Description
minimize	W_{fuel}	Total fuel consumption
	$\text{OASPL}_{\max}$	Maximum trailing-edge noise in LTO
with respect to	$\mathbf{x}_{\text{shape}}$	Shape variables
subject to	Range = Range*	Range requirement
	Payload = Payload*	Payload requirement
	Mission parameters = Parameters*	Altitude and speed requirements (refer to Fig. 3)

Fig. 2 depicts the complete process using the eXtended Design Structure Matrix (XDSM) representation[3] developed by Lambe and Martins [35]. In XDSM diagrams, thin black lines and thick gray lines represent the process flow and data dependencies, respectively. The analysis and optimization modules are shown in the diagonal entries of the XDSM "matrix". The inputs and outputs for each module need to be specified clearly, which are depicted as white parallelograms (for independent inputs) and gray parallelograms (for those passed between modules). Readers are referred to the original documentation [35] for details on the XDSM diagram conventions. The surrogate models for aerodynamics and aeroacoustics are initially constructed upon choosing the parameterization of the airfoil shape geometry. The geometry design variables are iteratively updated via the NSGA-II optimization algorithm until the minima are found.

4 Methodology

This section describes the methodologies used to construct the mission-based ASO framework presented in this paper. First, the flight performance analysis procedure is described in Section 4.1, with the corresponding aerodynamic and acoustic models being described in Section 4.2. The surrogate models used to represent airfoil geometry and the corresponding aerodynamic and aeroacoustic performance are described in Section 4.3. Finally, the method used to convert 2D airfoil data to appropriate 3D data that are used in flight mission analysis procedure is presented in Section 4.4, along with its validation.

4.1 Flight performance analysis procedure

The total fuel consumption, which is one of the objectives considered in this work, is calculated by the surrogate-based detailed mission analysis procedure developed by Lyu and Liem [36]. This framework was designed to be comprehensive, in that it takes airfoil geometry, mission parameters,

[3] https://github.com/mdolab/pyXDSM (last accessed on 18 December 2023).

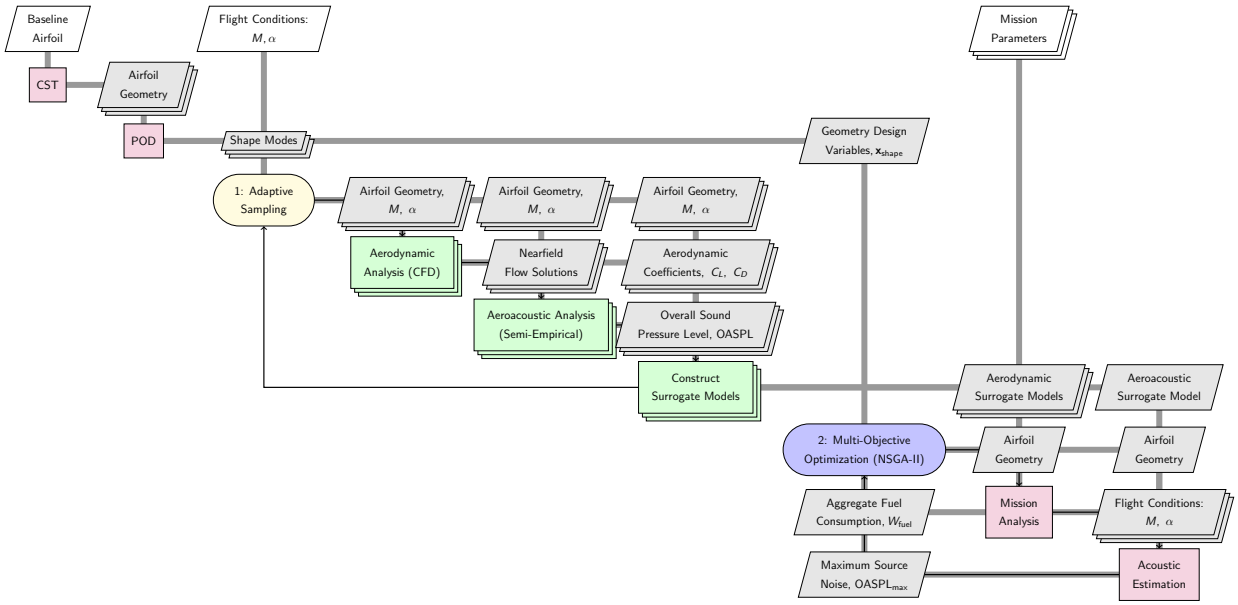
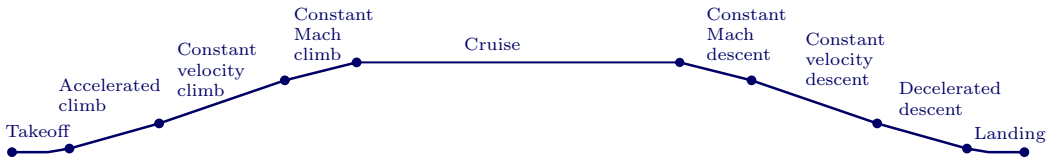


Figure 2: Overview of the mission-based airfoil shape optimization process. In this diagram, CST and POD refer to class-shape function transformation and proper orthogonal decomposition, respectively, which will be further explained in Section 4; NSGA-II and OASPL are as previously defined.

atmospheric conditions, engine, and aerodynamic models as model inputs and parameters to realistically assess aircraft performance for a given flight mission. To represent realistic flight operations, we define the mission profile by dividing it into five main segments—takeoff, climb, cruise, descent, and landing—as shown in Fig. 3.



h (ft)	0	35	10,000	31,500	35,000	35,000	31,500	10,000	35	0
V	0	150 KCAS	310 KCAS	310 KCAS	M 0.84	M 0.84	310 KCAS	310 KCAS	150 KCAS	0

Figure 3: Nominal mission parameters for the Boeing 777-300ER flights. The altitudes h are shown in ft, and the velocities V are shown in calibrated airspeed in knots (KCAS) or Mach number.

The mission analysis is built based on the generic range equation $R = \int_{t_i}^{t_f} V \, \mathrm{d}t$, the ordinary differential equation pertaining to fuel weight depletion $\mathrm{d}W/\,\mathrm{d}t = -c_T \cdot T$, and flight equilibrium equations. In these equations, t, V, W, T, and c_T refer to the time, velocity or airspeed, weight, thrust, and thrust-specific fuel consumption, respectively. Table 3 lists the types of segments and their corresponding governing equations to determine the distance covered, time taken, and weight depletion, i.e., the amount of fuel burned during flight, in this framework.

Table 3: Equations used for computing range, time, and weight over the different segments defined in the mission profile.

	Climb and Descent	**Cruise**	**Takeoff and Landing**	
			Ground Roll	**Climb/Descent**
Range	$\int_{h_i}^{h_f} \frac{V\cos\gamma}{RC}\,\mathrm{d}h$	$\int_{W_i}^{W_f} -\frac{V}{c_T T}\mathrm{d}W$	$\int_{V_i}^{V_f} \frac{WV}{g[T-D-\mu_r(W-L)]}\mathrm{d}V$	$\frac{h_{\mathrm{Ob}}-h_{\mathrm{TR}}}{\tan\gamma_{\mathrm{c}}}$
Time	$\int_{h_i}^{h_f} \frac{1}{RC}\,\mathrm{d}h$	$\int_{W_i}^{W_f} -\frac{1}{c_T T}\mathrm{d}W$	$\int_{V_i}^{V_f} \frac{W}{g[T-D-\mu_r(W-L)]}\mathrm{d}V$	$\frac{(h_{\mathrm{Ob}}-h_{\mathrm{TR}})\sin\gamma_{\mathrm{c}}}{1.2V_{\mathrm{stall}}}$
Weight	$\int_{h_i}^{h_f} -\frac{c_T T}{RC}\mathrm{d}h$	$\int_{W_i}^{W_f} \mathrm{d}W$	$\int_{V_i}^{V_f} -c_T T\frac{W}{g[T-D-\mu_r(W-L)]}\mathrm{d}V$	$-c_T T t_{\mathrm{cl}}$

The integrals shown in Table 3 are solved by means of numerical quadrature. The required performance parameters of the aircraft are T, lift L, drag D, and W. The subscript $(\cdot)_i$ denotes the initial value of a segment, while $(\cdot)_f$ represents the final value. The segments' end values are ensured to be consistent by solving a set of residual equations. h is the altitude of the aircraft, γ is the flight path angle, and RC is the rate of climb. The takeoff and landing phases can be further divided into two subsegments, namely ground roll and climb/descent. In these calculations, g is the gravitational acceleration, μ_r is the static friction coefficient, V_{stall} is the stall speed, γ_{c} is the climb angle, h_{TR} is the transition height, and h_{Ob} is the height of the obstacle. V is determined by the mission specification, and D is evaluated upon determining the flight conditions such as the angle of attack and flight path angle that satisfy the lift constraint. This D value determines T and hence the throttle setting, which affects c_T values. Solving the mission analysis yields the converged values of flight conditions at all integration points along the mission profile. For more details, readers are referred to the original paper [36].

The flight performance analysis is demonstrated on a long-haul flight mission flown with a Boeing B777-300ER aircraft, which is compatible with the CRM wing geometry. The mission specifications of the nominal mission profile are summarized in Fig. 3. The altitude h (in ft) and velocity V (in calibrated airspeed in knots [KCAS] or Mach) corresponding to each segment's end are shown underneath the mission profile. The connection between aerodynamic, flight performance, and TEN will be elaborated as follows. As mentioned above, the mission analysis requires aerodynamic forces L and D in the calculation. Upon analyzing the full mission, we can obtain total fuel consumption by calculating the difference between the initial and final mission weights. In addition, this procedure evaluates the corresponding flight conditions at different points along the mission profile, where the physical consistency is inherently enforced by the governing equations. Among these flight conditions, angle of attack α and Mach number M (shown in Fig. 4) will be used in the noise calculation. Although only the low Mach region (corresponding to the LTO phase) is considered for TEN evaluation in this paper, this mission analysis framework can provide a platform to assess flight noise over the entire flight mission. This will particularly be relevant to

the analysis and design of supersonic aircraft, where the noise impact remains substantial at a high altitude [37]. This extension, however, is beyond the scope of this paper.

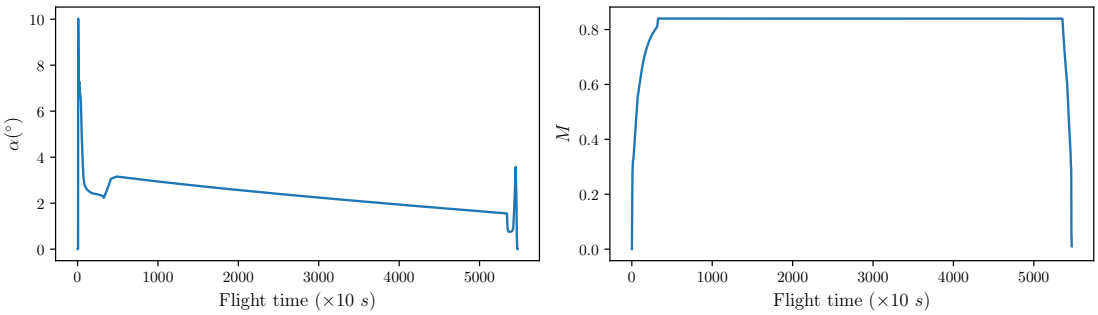


Figure 4: Detailed flight information generated from the mission analysis.

4.2 Physics-based models for aerodynamic, propulsive, and trailing-edge noise estimation

The computations of aerodynamic and propulsive forces are required to evaluate the performance of the aircraft, particularly fuel consumption. In Section 4.2.1, we briefly describe the physics-based aerodynamic model (using CFD) and the propulsion model used to estimate these quantities. Upon completing CFD analyses, we obtain some parameters needed to evaluate TEN, which is described in Section 4.2.2. The verification and validations of these physics-based models are presented in Section 4.2.3.

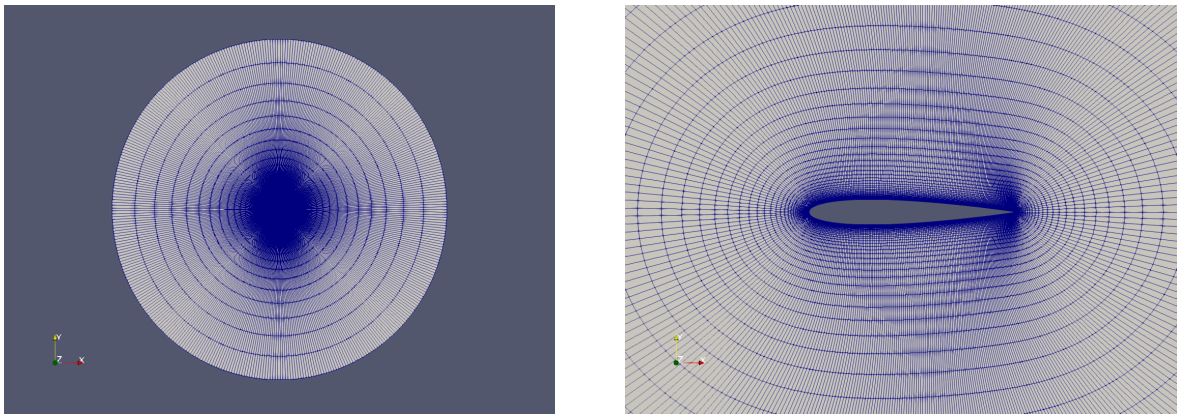
4.2.1 Estimation of performance parameters

In this research, CFD simulations are used to estimate the aerodynamic coefficients of the airfoil. Detailed information of the flow over the airfoil obtained from these simulations is then used for noise prediction by using a hybrid method. To this end, RANS-based models are considered sufficient to correctly predict TEN trends, as they are able to reflect minor changes in the design variables such as freestream velocity or geometric modifications [38].

The CFD simulations are performed with the open-source SU2 CFD solver[4], using the well-established Menter's Shear Stress Transport (SST) turbulence model to close the two-dimensional RANS governing equations [39]. The CFD simulation is considered converged when the variation of drag coefficient over 100 iterations is lower than 5×10^{-6}, which indicates sufficient accuracy. The grids for the analyses are generated using the open-source software `Construct2D`[5]. The domain of the grid extends to 150 chord lengths from the airfoil surface, as shown in Fig. 5. The CFD simulation results provide estimations of $y^+ \approx 1$, indicating appropriate grid resolution with the SST turbulence model.

To estimate thrust T and thrust-specific fuel consumption c_T, an engine surrogate model is

[4] https://su2code.github.io/ (last accessed on 15 February 2024).
[5] https://sourceforge.net/projects/construct2d/ (last accessed on 15 February 2024).



(a) Grid overview for NACA0012.

(b) A close-up of the grid around a NACA0012 airfoil.

Figure 5: A sample mesh generated by Construct2D.

generated based on Boeing 777-300ER data using the open-source SMT: Surrogate Modeling Toolbox [40]. The model inputs include flight altitude, Mach number, and throttle setting. The throttle setting for the cruise phase is determined by equating thrust to drag for level flight, and it follows PIANO-5 [41] for the rest of the flight phases.

4.2.2 Airfoil trailing-edge noise prediction

Ideally, an unsteady flow simulation is required to predict TEN. To simplify the calculation, a well-established alternative method is to use a WPS model that can estimate the acoustic performance of an airfoil based on steady flow information, such as flow boundary characteristics and airfoil surface pressures. This WPS can then be utilized as input for the acoustic model to predict the far-field noise. In this paper, a well-proven model developed by Kamruzzaman [42] is used for modeling the WPS. This model is derived based on various airfoil shapes with different angles of attack and Reynolds numbers. For all the cases examined, the accuracy for the maximum noise level is at ±1 dB. The universal WPS equation is given as follows:

$$\Phi(\omega)S_s = \frac{a(\omega F_s)^b}{\left[i(\omega F_s)^c + d\right]^e + \left[\left(fR_T^g\right)(\omega F_s)\right]^h}, \tag{1}$$

where Φ is the power spectral density of surface pressure fluctuations and ω is the angular frequency. S_s and F_s are the scaling factors for spectrum and angular frequency, respectively. The coefficients a to i are parameters whose values depend on the TEN model formulation. Interpreting the parameter physically, a modulates the spectral amplitude and is determined by the wake parameter Π_c, Clauser's parameter β_c, and the boundary layer shape factor H_{12}, which are calculated by Eq. (3). The remaining parameters b to i are constants obtained from experimental data fitting, where b, c, e, and h control the slope of the spectrum at different frequencies, f and g affect the onset of the transition between the overlap and high frequency, d affects the location of the low-frequency

maxima, and i is set to 1.0 for all models. The ratio of time scales can be expressed as

$$R_T = \frac{\delta^*/U_e}{\nu/u_\tau^2}, \tag{2}$$

where δ^* is the boundary-layer displacement thickness, U_e is the velocity at the boundary-layer edges, ν is the kinematic viscosity, and $u_\tau = (\tau_\omega/\rho)^{1/2}$ is the friction velocity. τ_ω denotes the shear stress at the wall and ρ is the density of the fluid. Table 4 lists the coefficients used in Kamruzzaman's model [42].

Table 4: Parameters for the semi-empirical wall-pressure spectrum model.

a	b	c	d	e	f	g	h	i	S_s	F_s
$0.45\left[1.75\left(\Pi_c^2\beta_c^2\right)^m + 15\right]$, where $m = 0.5\left(H_{12}/1.31\right)^{0.3}$	2.0	1.637	0.27	2.47	$1.15^{-2/7}$	$-\frac{2}{7}$	7.0	1.0	$\frac{U_e}{\tau_\omega^2\delta^*}$	$\frac{\delta^*}{U_e}$

The parameter β_c is obtained by the curve-fit proposed by Nash [43], where G is the parameter of the G-β_c locus, and C_f is the skin-friction coefficient. The calculations of these parameters are shown below,

$$G = 6.1\sqrt{\beta_c + 1.81} - 1.7,\ H_{12} = \left(1 - \frac{G}{\lambda}\right)^{-1},\ \lambda = \sqrt{\frac{2}{C_f}},\ \Pi_c = \begin{cases} 0.8\left(\beta_c + 0.5\right)^{\frac{3}{4}} & \beta_c > -0.5 \\ 0.227 & \beta_c \le -0.5 \end{cases}, \tag{3}$$

where λ is just a symbol used to simplify the expression involving C_f.

Once the WPS is calculated, we can use this to calculate the far-field acoustic spectrum. In this paper, we utilize a model developed by Howe [29], which is valid for low Mach region. This model considers an observer positioned above and perpendicular to the trailing edge ($\Theta_e = 90°$). This equation is given below,

$$G_{ff}(\omega) = \frac{1}{4}\left(\frac{L_y}{\pi^2 R_x^2}\right)\left(\frac{Ma_c}{1 - Ma_c}\right)\Lambda_3(\omega)\Phi(\omega), \tag{4}$$

where $G_{ff}(\omega)$ denotes the acoustic spectrum, $Ma_c = U_c/c_0$ is the convective Mach number (here, U_c is the mean convective velocity of wall pressure fluctuations and c_0 is the speed of sound), R_x is the observer distance, L_y is the span-wise length of the airfoil, and Λ_3 is the span-wise coherence integral length scale of pressure. The wall-pressure spectrum $\Phi(\omega)$ is calculated from Eq. (1). Blake showed that the assumption $U_c = 0.7U_\infty$, where U_∞ is the inflow velocity, was deemed reasonably sufficient for modeling purposes [30]. Corcos' model is adopted for the span-wise length scale Λ_3 [29], which is shown below,

$$\Lambda_3 = \frac{U_c}{\gamma_3\omega},\ \text{where } \gamma_3 = 1. \tag{5}$$

The far-field noise spectrum needs to be reduced to a single representative value for the optimization objective. In this case, we use the sound pressure level (SPL), which indicates the effect

of the source noise propagated to an observer perpendicular to the trailing edge of the airfoil [44]. The one-third octave-band spectrum of the SPL is calculated using Eq. (6),

$$\begin{aligned} SPL(f) &= 10\log_{10}\left[10^{0.1L_{p,ps}} + 10^{0.1L_{p,ss}}\right], \text{ where} \\ L_{p,ss} &= 10\log_{10}\left[\frac{2\pi G_{ff}(\omega)\cdot \mathrm{d}f}{P_{\text{ref}}^2}\right], \quad P_{\text{ref}} = 2\times 10^{-5} Pa. \end{aligned} \tag{6}$$

In this equation, $L_{p,ss}$ and $L_{p,ps}$ are the suction side spectrum and pressure side spectrum, respectively. P_{ref} is the reference pressure. Instead of using the third-octave spectrum of SPL directly, a suggested approximate value is the A-Weighted OASPL, which has been used widely to assess human perceptions/sensitivities to sound [44]. A-weighting is employed by adding a table of octave or third-octave band values to the measured sound pressure levels in dB. Hence, the A-weighted OASPL is chosen as the quantity of interest for the optimization cases presented herein. We note that since only two points on the airfoil are evaluated for the noise spectrum, the calculated value may only partially represent the overall airfoil noise. This study primarily aims to determine the effects of noise when considered in a shape optimization problem in a mission-based framework. The extension of the work to reduce the entire noise generated by the shape is a subject of future work.

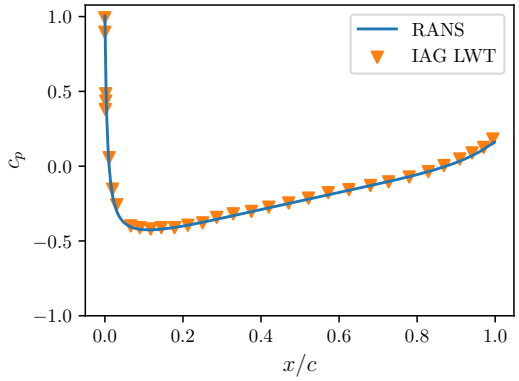
4.2.3 Verification and validation of physics-based models

An existing wind tunnel test case from the Benchmark Problems for Airframe Noise Computations (BANC) workshop [26] is selected to validate the aerodynamic and acoustic prediction models presented in Section 4.2.1 and Section 4.2.2. This case has been widely referred to in previous research [42, 31, 44] for validation purposes. The A-weighted OASPL result is also validated against results from a previous study [44].

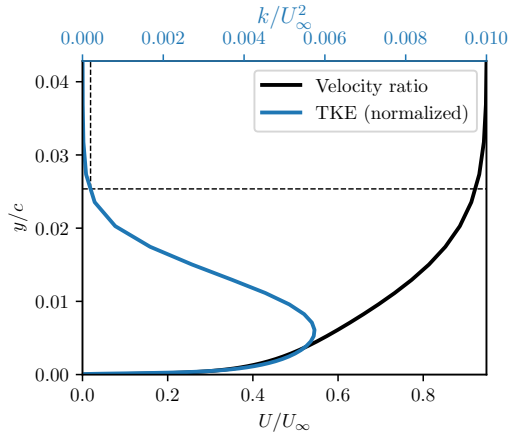
The BANC test case used in this study considers a 2D NACA 0012 airfoil section in a nominally uniform flow, which is characterized by the mean flow velocity $U_\infty = 56$ m/s and an angle of attack $\alpha = 0°$. In this experiment, the operating Mach number and Reynolds number are set to $M = 0.1664$ and $Re = 1.5 \times 10^6$, respectively, where chord length $c = 0.4$ m and mean ambient density $\rho_\infty = 1.181$ kg/m^2 are used in the Reynolds number calculation. The trailing-edge point location is set to be at the chord position $x/c \approx 0.99$ for measurement purposes. The span is assumed to be 1 m for the acoustic analysis, and the measurement is performed 1 m directly above this trailing-edge point.

To validate the models, the CFD simulations are set to match these experimental conditions. Fig. 6 demonstrates various validation cases, with orange symbols depicting the experimental data and blue lines depicting the predictions from the physics-based models. Fig. 6a shows the pressure coefficient c_p distribution. The orange inverted triangles show available measurement data from the Laminar Wind-Tunnel (LWT) at the Institute of Aerodynamics & Gas Dynamics (IAG) [26], and the blue line represents the solutions computed via CFD. As shown in Fig. 6a, the c_p distribution exhibits a high degree of accuracy. Fig. 6b plots the boundary layer profile normal to the airfoil

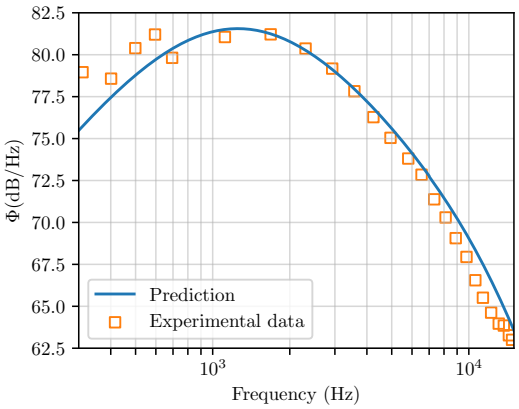
surface against the local velocity. The blue line refers to the kinetic energy over the square of the local freestream velocity, where the values are indicated in the upper x-axis. The black line shows the velocity profile in the boundary layer, which is indicated by the lower x-axis. The boundary layer thickness is detected via the Catlett's approach [45]. In this method, the boundary layer thickness is defined as the normal distance from the airfoil surface to a point where the turbulence kinetic energy (TKE) $k = 0.0002U_0^2$, with U_0 being the freestream velocity. This boundary layer thickness value is then used to determine the boundary layer edge velocity U_e. Upon determining the boundary layer thickness, the boundary layer parameters can be determined from the equations presented in Section 4.2.2.



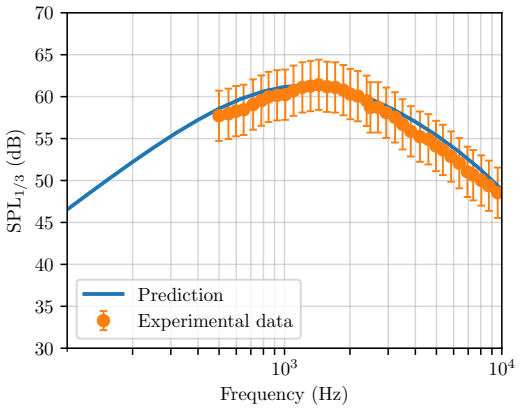
(a) Validation of pressure coefficient c_p distribution from CFD simulations



(b) Boundary layer thickness determination from the Catlett's approach



(c) Validation of wall-pressure spectrum prediction



(d) Validation of far-field noise spectrum prediction

Figure 6: Validation of aerodynamic and acoustic models for a NACA 0012 airfoil case.

Fig. 6c depicts the WPS prediction calculated using the Kamruzzaman's model [42]. The orange squares denote experimental data extracted from the BANC workshop [26], and the blue line is the prediction obtained from following the method proposed by Küçükosman *et al.* [22], indicating sufficient accuracy. Fig. 6d depicts the far-field acoustic spectrum predicted using Howe's model

and the measurement data from the BANC workshop. Depending on the experimental facility and equipment, the measurement noise data may vary by ±3 dB for the same airfoil, which is depicted by the orange bars. The OASPL is 70.974 dB(A) for this validation case, whereas it is 71.20 dB(A) in the work by Ricks *et al.* [44]. The minor difference may come from the adoption of different analytical models for noise propagation, as Ricks *et al.* utilized Amiet's model to generate their results.

The validation results presented above show a satisfactory level of agreement with previous experimental references, concerning both aerodynamics and aeroacoustics. The high level of accuracy provides confidence in using these models in subsequent analyses and optimization. In the following surrogate model derivation, these models will be used with the same computational setup as that of the validation process, and we only change the flow conditions and airfoil geometries for sampling purposes.

4.3 Surrogate modeling approach

The computational cost of solving an optimization problem depends on the number of design variables, which indicates the problem complexity, as well as the number of required objective function and constraint evaluations. Using a gradient-free algorithm to solve the mission-based optimization (Section 3.2.2) can incur a high computational cost. To alleviate this computational burden, we couple a model order reduction approach with a commonly used airfoil geometry parameterization method to reduce the number of shape design variables in the problem; this approach will be described in Section 4.3.1. Additionally, the evaluations of flight conditions in the discretized mission profile also require thousands of lift and drag calculations. However, using CFD to calculate these forces is expensive, where the computational time can range from minutes to hours depending on the complexity and fidelity of the analysis, which renders it impractical for the specific problem at hand. Hence, to perform ASO efficiently in this mission-based context, surrogate models are constructed to yield inexpensive approximations of the relevant physics-based models, which will be described in Section 4.3.2. In particular, surrogate models are utilized to determine the aerodynamic and engine performance parameters by training the models using CFD simulation and experimental data. These surrogate models are generated offline and will be used to evaluate the optimization objectives at a relatively low computational cost.

4.3.1 Model order reduction of geometry parameterization

Airfoil parameterization methods can be broadly categorized into two groups, namely constructive approaches, such as class-shape function transformation (CST) [46]; and deformative approaches, such as free-form deformation (FFD) [47]. In general, both types of methods require more design variables to represent airfoil shapes more accurately with less restrictions in the design space, at the expense of increased computational cost. To alleviate this issue, further reducing the problem dimensionality is imperative.

Proper orthogonal decomposition (POD) is a suitable solution to address this problem, by

transforming a set of candidate airfoils in the design space into a set of orthogonal shape modes. By considering only the most dominant modes, it can effectively reduce the number of design variables while maintaining the ability to represent various airfoil shapes. The effectiveness of a POD-based CST parametric method has been verified on a benchmark ASO problem by Wu *et al.* [48]. The result showed that this deformative parametric approach could cover almost the same level of deformation with fewer than half of the number of original CST design variables, thereby reducing the dimensionality of the design space while maintaining accuracy.

In this paper, we employ the POD-based CST parametric method [48], as described briefly below. Upon performing the high-dimensional CST parameterization, we generate a set of random sampling snapshots of the CST variables within the design space. Let $\mathbf{S} = \begin{bmatrix} \mathbf{s}_1 & \mathbf{s}_2 & \dots & \mathbf{s}_i & \dots & \mathbf{s}_p \end{bmatrix}$ be the matrix of p snapshots, with states $\mathbf{s}_i \in \mathbb{R}^k$ as column vectors for $i = 1, \dots, p$, where k is the dimension of $\mathbf{s}$. We then select l POD modes, where $l \ll \min(k, p)$, through the truncated singular value decomposition. Using this approach, the upper and lower surface of the airfoil can be expressed as a linear combination of the eigenvectors $\mathbf{v}$ (also called modes) as perturbations from the average (or mean) shape $\bar{\mathbf{s}}$, as shown below,

$$\mathbf{s} = \bar{\mathbf{s}} + \sum_{i=1}^{l} \alpha_i \mathbf{v}_i, \text{ where } \bar{\mathbf{s}} = \frac{1}{p} \sum_{i=1}^{p} \mathbf{s}_i.$$

This method is applied to our baseline airfoil (i.e., the CRM eta65 airfoil), which was described in Section 3.1. The least-square fitting to find the corresponding CST variables is shown in Fig. 7. Here, the CRM eta65 airfoil geometry is described by 20 variables with the ninth-order Bernstein polynomials (BPO9) analytical expression. Following the work by Long *et al.* [49], we define the bounds of the CST variables b_i as

$$0.8 b_{i\ \text{(initial)}} \leq b_i \leq 1.2 b_{i\ \text{(initial)}} \quad (i = 1, 2 \cdots, 20)\,. \tag{7}$$

Note that these bounds apply to both upper and lower surfaces of the airfoil.

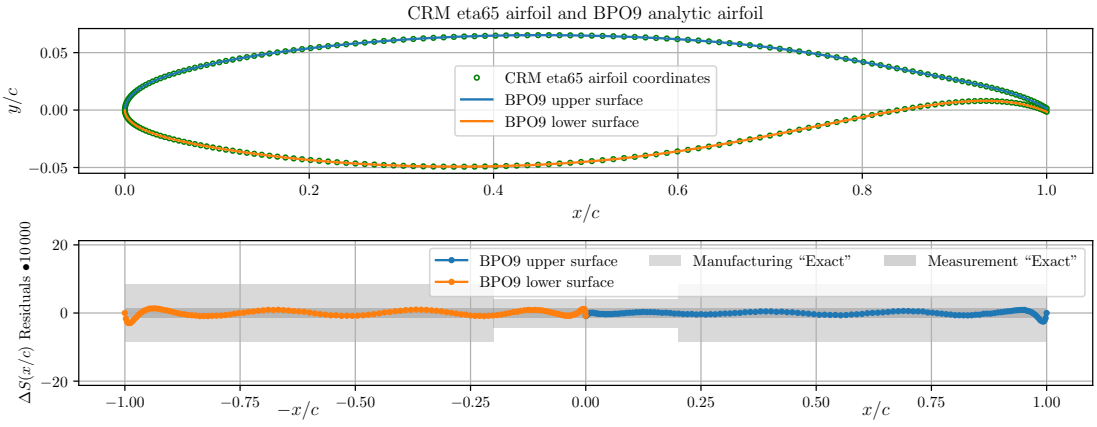
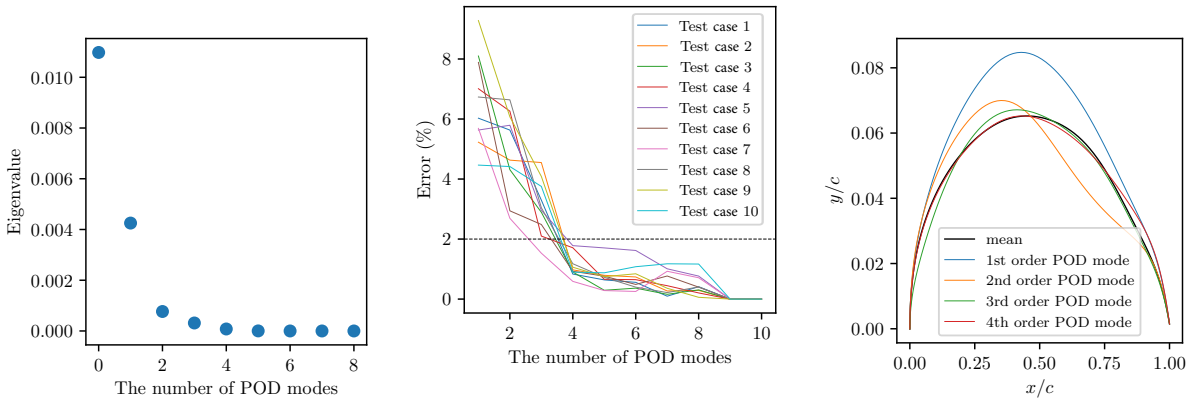


Figure 7: CRM eta65 geometric representation and surface coordinate residuals.

To assess the accuracy and effectiveness of POD, we consider the upper surface of the baseline airfoil as an illustration, which is depicted by the blue line in Fig. 7. Based on the exactness condition defined by Kulfan [46], ten CST parameters—including nine parameters that define the BPO9 and one parameter that determines *nose slope*—are extracted to represent the geometry to the desired accuracy. By altering these parameters in the design space, we generate a set of upper surface geometries as sample snapshots, which are further used to determine the singular values and eigenvectors (modes) through the POD analysis. Fig. 8a shows the eigenvalues and the corresponding modes, where the first four modes account for 99.5% of the complete information. This indicates that the first four POD basis functions can achieve almost the same descriptive ability as the full BPO9 representation. To further validate this observation, we randomly select ten test cases for the upper surface of the airfoil and analyze their approximation errors. As shown in Fig. 8b, the errors between the POD-based CST description and BPO9 expression for test cases 1 to 10 decrease as the number of POD modes increases. These results also show that using four POD modes can achieve an accuracy of 98%, which is sufficient to substitute the original CST method.



(a) The eigenvalues with the number of modes

(b) Error analyses of ten randomly selected test cases, for validation purposes.

(c) The deformation of the first 4 POD modes

Figure 8: The POD analysis of the upper surface of CRM eta65 airfoil.

The first four POD modes, which indicate the deformation of airfoil shapes, are depicted in Fig. 8c. There is a negative correlation between the modal order and the importance in the POD method. Mode one generates a scaled-up deformation of the upper surface shape perpendicular to the chord direction, while mode two changes the position of the maximum thickness. The deformations tend to be less prominent as the modal order increases. By using the same procedure for the lower surface of the airfoil, the POD-based CST mathematical expression can represent the CRM eta65 airfoil with just eight variables. It is noted that all the sample snapshots are selected based on the CST design space, which is shown in Eq. (7). Therefore, the bounds of the POD variables remain consistent with the CST bounds.

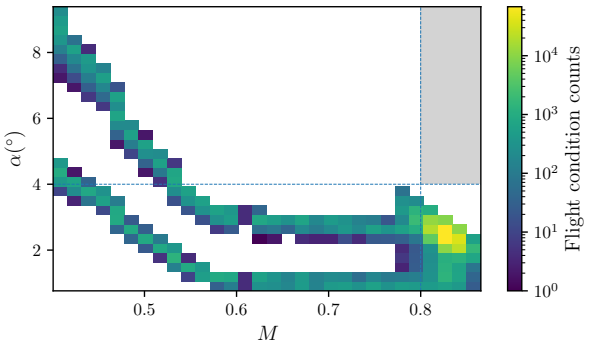


Figure 9: The distribution of angle of attack and Mach number obtained from the data-enhanced mission analysis procedure.

4.3.2 Surrogate model construction for aerodynamic coefficients and noise metric

Sample selection is an important component in surrogate model construction. First, the appropriate bounds need to be determined for each variable, such that the drawn samples would fall within the appropriate design space. The bounds for the geometry variables have been established in Section 4.3.1. In this section, the determination of the bounds for the remaining variables, namely α and M, is described.

To ensure that the selected bounds are consistent with actual flight operations, the flight-condition distribution generated in a previous study [36], which is shown in Fig. 9, is used as reference. Note that the flight conditions extracted herein are based on the M and α values of a 3D CRM wing model obtained from analyzing given mission specifications and profiles using the flight mission analysis procedure described in Section 4.1. Their conversion to the flow condition values pertaining to the corresponding 2D airfoil cross section will be given in Section 4.4. This distribution corresponds to a long-haul flight, to be consistent with the flight mission chosen for the mission-based optimization presented herein. The gray area, where no flight condition is observed, is excluded from the design space to eliminate the need to perform aerodynamic analyses at a high M, high α region. Indeed, performing CFD analyses at such a flight condition is not practical due to the presence of a transonic buffet (aircraft vibration phenomenon due to shock-wave oscillation), especially at a high α. Therefore, performing RANS simulations under high α is prone to non-convergence in the transonic region. To avoid performing impractical and unnecessary CFD simulations, the maximum α is constrained to 4° in the transonic region, whilst the limit is 10° elsewhere. By referencing the operational data, the bound of M is defined to be from 0.1 to 0.86. For the A-weighted OASPL surrogate model, M is set to be from 0.1 and 0.25 due to the limitation of the acoustic model. Recall that we only consider the LTO phases for TEN calculation, which only concerns low Mach operations, so this value bound is deemed reasonable. It is worth noting that the full range of M values, $0.1 \leq M \leq 0.86$, is considered in the flight mission analysis, from which we obtain the corresponding flow conditions needed to evaluate the noise metric.

To construct the surrogate models more efficiently, we adopt an adaptive sampling approach

which starts with an initial set of training data, followed by building the initial surrogate model. In particular, the well-established Latin Hypercube Sampling (LHS) [50] is applied to find the initial airfoil samples. Afterward, additional sample points are added to the dataset by successive iterations following the space-filling cross-validation tradeoff method until the convergence or stopping criteria are reached [51]. The sizes of training and testing datasets are listed in Table 5, and there are no overlaps between these two datasets. Ordinary Kriging[52] is chosen to approximate the aerodynamic and aeroacoustic predictions. For the three surrogate models built, their root mean square errors (RMSEs) are all less than 4%, as shown in Table 5. This level of accuracy is deemed sufficient for the specific problem at hand.

Table 5: Surrogate model specifications for constructions and validation.

	Model type	Number of samples	Number of test cases	RMSE
C_L	Kriging	85	4,415	2.853%
C_D	Kriging	93	4,407	3.961%
SPL	Kriging	98	4,402	2.354%

4.4 Validation of fuel consumption calculation based on airfoil's aerodynamic data

In this section, we will describe how the aerodynamic values of 2D airfoil are appropriately used in the flight mission analysis to evaluate fuel consumption, along with its validation. In particular, we follow the conversion procedure provided by NASA[6], which has been derived and validated specifically for a CRM wing model.

Recall that the 3D CRM wing model is a sweptback wing (as shown in Fig. 1, Section 3.1). Hence, we first need to convert the flow conditions, namely Mach number M and Reynolds number Re, using Eq. (8) and Eq. (9) (from the NASA procedure mentioned above), respectively,

$$M_{2D} = M_{3D} \cos 31.5^\circ \tag{8}$$

$$Re_{2D} = Re_{3D} \cos 31.5^\circ = Re_c \frac{C.65}{C_{\text{ref}}} \cos 31.5^\circ \tag{9}$$

where M_{3D} is the free stream Mach number of the 3D CRM wing, Re_{3D} is the sectional Reynolds number of the CRM eta65 airfoil for a reference-chord Reynolds number Re_c, whereas M_{2D} and Re_{2D} refer to the corresponding Mach and Reynolds numbers for the 2D case. The chord length of the selected airfoil is denoted as $C.65 = 206.5$ inches (5.2451 m), and the reference chord length of the wing is represented by $C_{\text{ref}} = 275.8$ inches (7.0053 m).

Next, we convert the lift coefficient of the 2D airfoil C_l to the corresponding sectional lift

[6] https://commonresearchmodel.larc.nasa.gov/crm-65-airfoil-sections/ (last accessed on 16 December 2023).

coefficient for the CRM wing at 65% span C_{ls3D} by using the following conversion,

$$C_l = \frac{C_{ls3D}}{\cos^2 31.5°}. \tag{10}$$

To obtain the corresponding lift coefficient pertaining to 3D wing C_L, a simple multiplication factor is applied, i.e., $C_L = 1.14 \times C_{ls3D}$, following the NASA guidelines mentioned above. To obtain the drag coefficient for the 3D wing C_D, we add an induced drag component $C_{Di} = \frac{C_L^2}{\pi AR}$ to C_d (which is essentially the drag coefficient of an infinite wing). Hence, $C_D = C_d + C_{Di}$. The obtained "pseudo" 3D values are then compared against the aerodynamic coefficients computed based on the 3D wing model, which are shown in Fig. 10. The RMSEs for C_L and C_D are 1.451% and 3.783%, respectively, which provide sufficient accuracy for our subsequent computations.

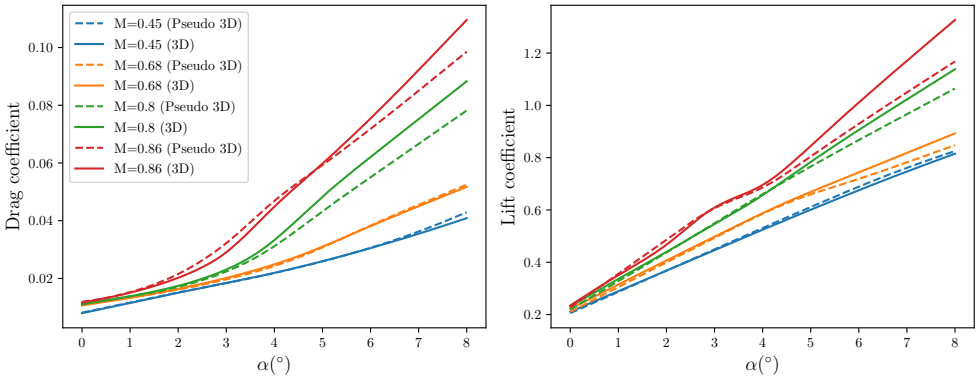


Figure 10: Aerodynamic performance comparison between the calculated "pseudo" 3D values and those obtained from the 3D CRM wing for selected representative flight conditions

.

Lastly, we validate the use of "pseudo" 3D aerodynamic coefficients in the flight mission analysis (as described in Section 4.1) to evaluate fuel consumption. The validation is performed on 1,046 long-haul flights, which are modeled using the parameterized mission and speed profiles that are consistent with those presented in [36]. The calculated fuel consumption values are compared against actual fuel burn data shared by our airline partner. Note that the actual fuel consumption values cannot be shown for confidentiality reasons, as stipulated in the agreement with our airline partner. Instead, some relative values (e.g., in percentage, ratio, or normalized) will be presented as appropriate. This validation process yields an RMSE of 4.165%, which is considered accurate for the specific problem at hand.

Having validated the aerodynamic coefficient calculations, these calculation and conversion methods will be used to obtain the optimization results presented in the next section.

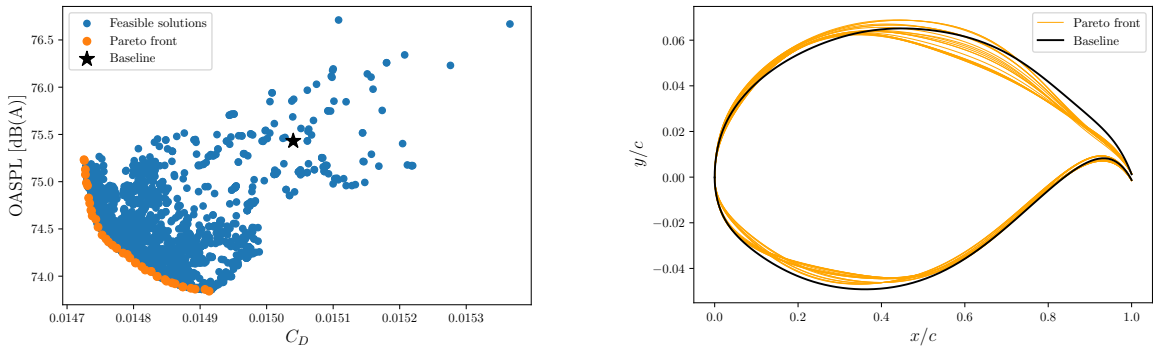
5 Framework applications and results

The developed mission-based optimization framework enables the investigation and exploration of the effect of considering TEN, in addition to aerodynamic performance, in an airfoil shape optimiza-

tion problem. In particular, the framework makes it possible to study the tradeoff between noise and fuel considerations, while taking into account the comprehensive flight operational spectrum of the aircraft. To compare the new mission-based optimization with the traditional approach, we also perform a single-point optimization, as described in Section 3.2. Both optimizations are performed with the NSGA-II algorithm. In these cases, the population size is 40 and the maximum evaluation budget is 8,000. Based on our preliminary experiments, these quantities are deemed sufficient to provide a well-defined Pareto front for both cases. The convergence metric is set based on the minimum Euclidean distance from each solution obtained to the chosen points on the Pareto-optimal front. For all cases presented in this paper, the Pareto front converges before reaching the maximum number of evaluations. More detailed results and discussions are presented below.

5.1 Single-point optimization results

The results obtained from applying the single-point optimization formulation described in Section 3.2.1 are presented in Fig. 11. In Fig. 11a, orange dots represent the Pareto front and feasible solutions, whereas the black star denotes the baseline design. The corresponding optimal airfoil shapes are shown by the orange lines in Fig. 11b. In contrast to the baseline airfoil, which is represented by the black line, the optimized airfoils exhibit a relatively higher profile gradient along the upper surface, starting from the bow section to the trailing edge. In addition, the optimum airfoils show a consistent decrease in OASPL compared to the baseline airfoil. However, despite this improvement, the impact of the optimized airfoils on drag coefficient reduction is relatively small, as shown by the horizontal distance between the baseline and Pareto points in Fig. 11a.



(a) Pareto front of single-point, multi-objective optimization

(b) Airfoils generated in the Pareto optimum set

Figure 11: Single-point optimization results.

To more comprehensively evaluate the performance of the optimum airfoils, we calculate the corresponding total fuel consumption (using the flight mission analysis procedure) and maximum TEN (during LTO operations). The resulting discrepancies between the optimized airfoils and the baseline case are illustrated in Fig. 12, where the blue bars indicate the relative fuel consumption ratio and the orange bars indicate the relative TEN. Here, a negative value is desirable as it corre-

sponds to fuel or TEN reductions in the optimized results. As shown, all optimized airfoils exhibit improved performance with respect to noise reduction. However, the computed fuel consumption is consistently higher than that of the baseline case, which demonstrates the fuel-noise tradeoff. To further elucidate this phenomenon, the airfoil with the most significant reduction in maximum TEN is selected for further investigation, which will be described below.

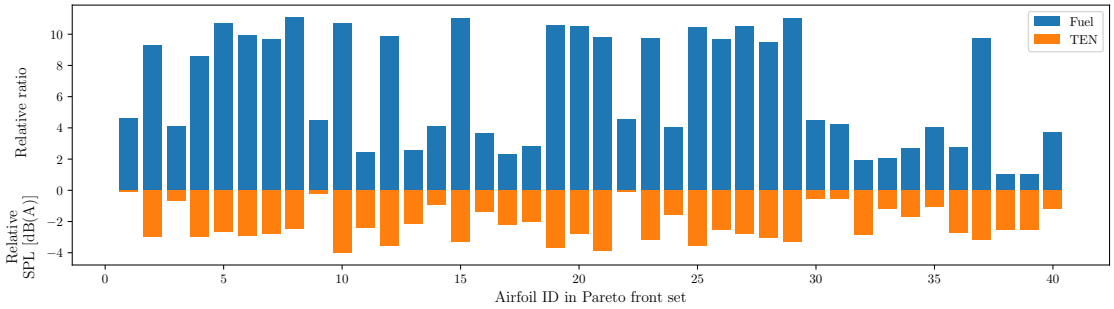
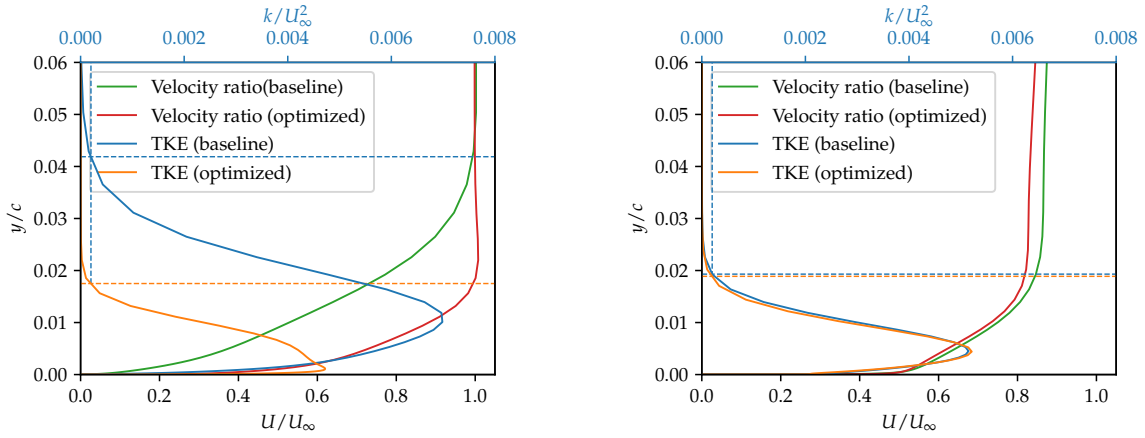


Figure 12: Relative ratio of fuel consumption and trailing-edge noise of single-point optimization results.

The mechanism behind OASPL reduction is found to be mostly related to a decrease in TKE across the boundary layer near the trailing edge. As shown in Fig. 13, while the TKE distributions of the baseline and selected optimum airfoils are quite similar, there is a notable reduction on the suction side. This reduction could be caused by the decambering of the airfoil and the flattening of the airfoil thickness near the trailing edge.



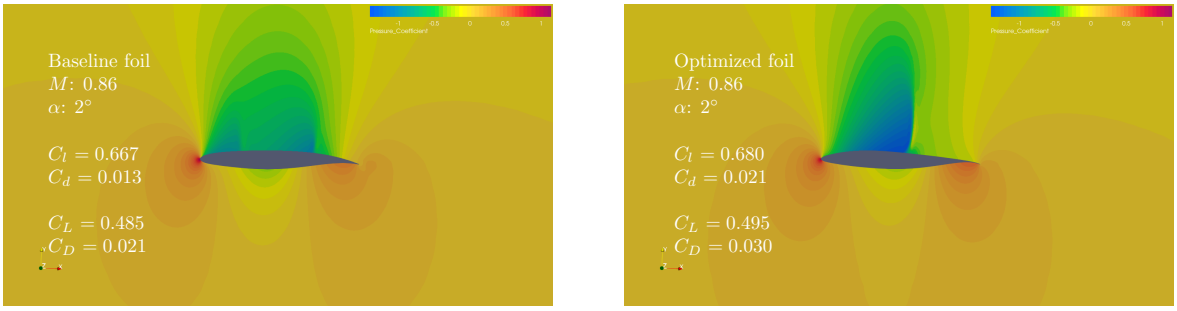
(a) Boundary layer thickness of the suction side

(b) Boundary layer thickness of the pressure side

Figure 13: Boundary layer characteristics of the selected optimum airfoil compared with baseline airfoil, conducted under the flow condition specified in Table 1.

To investigate the limitations of single-point optimization, the airfoil performance at *off-design* condition is analyzed. In particular, the case is purposely run to evaluate the airfoil performance under the transonic flow condition, which is notably different from the flight condition considered

in the single-point optimization formulation (i.e., within the LTO phase). Fig. 14 shows the aerodynamic and aeroacoustic performance of an airfoil selected from the Pareto optima at this transonic flow condition, where $M = 0.86$. C_l and C_d displayed in the plots refer to the lift and drag coefficients for the two-dimensional airfoil. Before using these quantities in the flight performance analyses, they are converted to the corresponding three-dimensional values (C_L, C_D) by using the conversion method described in Section 4.4.



(a) Baseline airfoil in transonic flow

(b) Optimized airfoil in transonic flow

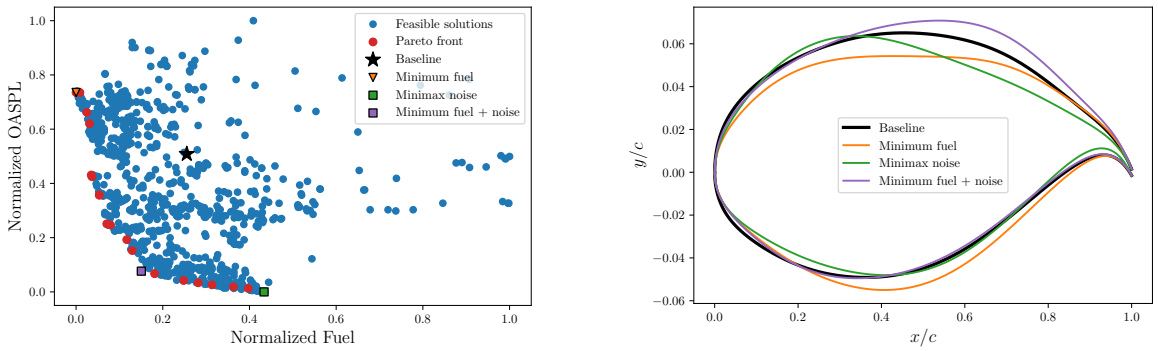
Figure 14: The pressure distribution of the selected optimum airfoil compared with baseline airfoil. Note that the case is run under the transonic flow condition, which is different from the flow condition considered in the single-point optimization formulation, to demonstrate its suboptimal performance at an *off-design* condition.

As can be seen in Fig. 14, the optimized airfoil's C_l is slightly higher than that of the baseline case; however, its C_d is also notably higher, thereby resulting in lower L/D and potentially contributing to more fuel consumption in the cruise phase, which is undesirable. This explains the increased fuel consumption shown in Fig. 12. With relatively better aerodynamic performance in the low Mach region, the fuel consumption with the optimized airfoil may be less than the baseline case's in the climb phase by design. In typical flight missions, however, fuel consumption during cruise accounts for the majority of the total fuel consumption, as previously observed [36, 53]. Despite the potential fuel savings offered by the optimized airfoil in the low Mach region, the notable increase in fuel consumption due to its degraded performance in the transonic region will outweigh the benefits, especially so when the cruise segment is dominant. This observation highlights the limitation of a single-point optimization, which is known to yield suboptimal performance at *off-design* conditions [16, 32]. To address this problem, the mission-based optimization approach is evaluated in the following section.

5.2 Mission-based optimization results

This design problem solves the multi-objective optimization problem presented in Section 3.2.2 for minimizing total fuel consumption and maximum TEN. The fuel consumption is computed over the nominal mission for each airfoil generated during the optimization process. The noise is calculated at 6 m above the trailing edge of the airfoil shapes to represent the source noise. As mentioned in Section 3.2.2, the noise objective is to minimize the maximum noise during the LTO

cycle. Hence, a *minimax* scheme is implemented herein. The hybrid method chosen for the noise estimation requires the far-field noise to be calculated under low Mach number flows. By definition, it refers to the region where convection speed is always much less than the speed of sound [54]. From the work by Kamruzzaman *et al.* [42], the highest speed can be as high as 78.7 m/s, which is around 150 KCAS. According to a previous work with the same flight mission specifications and analysis procedure [36], all the speed values (at the altitude of 1,500 ft) in the extracted mean actual climb speed (from the airline's recorded flight data) are less than or equal to 150 KCAS. Therefore, the noise estimations are performed for altitudes under 1,500 ft, including takeoff, landing, climb, and descent flight phases.



(a) Pareto front from mission-based optimization (b) Comparison of baseline and optimized designs

Figure 15: Airfoil shape optimization results from the mission-based formulation. (The fuel consumption values are normalized for confidentiality reasons.)

The Pareto fronts obtained from performing mission-based optimization for the nominal flight are shown in Fig. 15a. As before, the black star represents the baseline case. The values shown in this plot are normalized to be between 0 and 1. All the airfoils in the Pareto fronts show at least one advantage in terms of TEN or fuel consumption. Two extreme cases that generate the minimum fuel consumption and minimax of TEN, respectively, are selected and the corresponding airfoils are shown in Fig. 15b (in orange and green, respectively). In addition, a balanced case that can simultaneously reduce fuel consumption and noise is also chosen for further discussion, which is shown in purple.

Not surprisingly, the minimum fuel consumption airfoil exhibits lower fuel consumption than the baseline case, but its generated source noise level is higher. The optimized airfoil (indicated in orange in Fig. 15b) has a flatter upper surface compared to the baseline one and a highly cambered aft section.

Unlike the single-point optimization results, the optimum results from mission-based optimization consider the aircraft performance throughout the entire flight. Instead of showing a single-point comparison as in Fig. 14, the present study demonstrates more detailed aircraft performance. The aerodynamic evaluation of the minimum fuel consumption airfoil is shown in Fig. 16 (in solid lines), which is compared to the baseline results (in dashed lines). All the aerodynamic coefficients are

generated from the surrogate models described in Section 4.3. Some combinations of M and α are selected to show the airfoil performance in different flight phases. As described in Section 4.4, the C_L and C_D values are converted from the corresponding airfoil's C_l and C_d values. It is noted that only the lift and drag from the clean wing are considered in the mission analysis calculation.

Compared with the baseline airfoil, the optimized airfoil yields higher C_L with lower C_D in the transonic region. The higher L/D potentially contributes to reducing fuel consumption in the cruise stage, which is often the most dominant flight mission phase, especially in medium- and long-haul flights. Within the speed region where $M \leq 0.8$, most of the calculated C_L and C_D are lower than the baseline airfoil's results. However, the L/D ratio is still higher than that of the baseline airfoil. The higher L/D ratio over the entire range of flight conditions reduces the fuel consumption at each flight stage, as compared to the baseline case, thereby yielding a notable reduction in total fuel consumption.

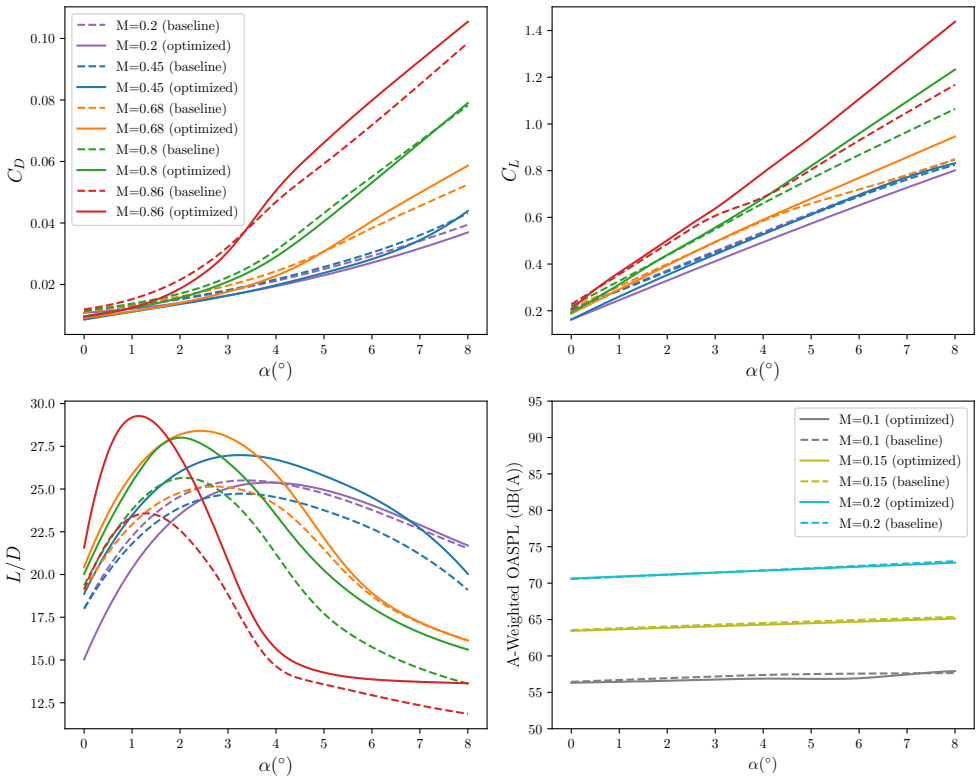
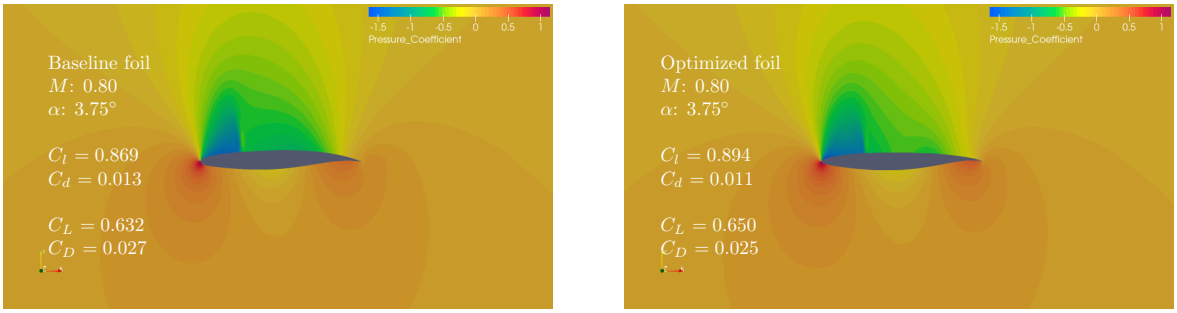


Figure 16: Aerodynamic and aeroacoustic performance comparison between minimum fuel airfoil and baseline airfoil for selected representative flight conditions

.

To further demonstrate the mechanisms underlying the enhanced aerodynamic performance, we conduct additional CFD analyses for both the baseline and minimum fuel airfoil under transonic flow conditions. As depicted in Fig. 17, the optimized airfoil features a flatter upper surface and a more refined trailing edge. These characteristics contribute to smoother pressure gradients on the upper surface, aiding in the delay of flow separation and the reduction of drag. Moreover,

the optimized design more effectively manages adverse pressure gradients, ensuring that the flow remains attached for a longer duration, thereby enhancing lift while simultaneously reducing drag.

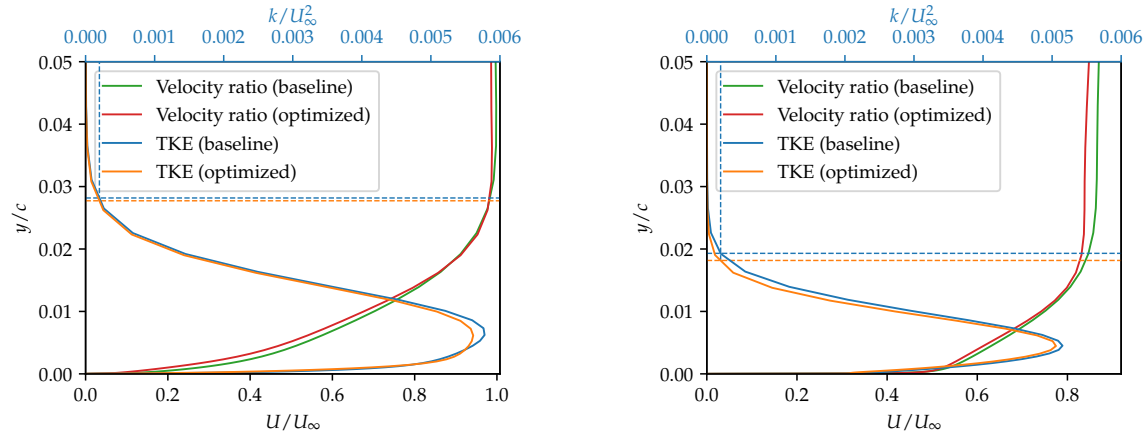


(a) Baseline airfoil in transonic flow

(b) Optimized airfoil in transonic flow

Figure 17: The pressure distribution of the minimum fuel airfoil compared with baseline airfoil.

In contrast with the aerodynamic performance improvement, we observe no notable improvement in terms of the aeroacoustic performance, as compared with the baseline case under the same flow condition. In the low Mach region, the optimized airfoil shows a relatively similar A-weighted OASPL compared with the baseline airfoil, as shown in the bottom right of Fig. 16. In this figure, the dashed lines show the TEN emissions from the baseline case, and the solid lines represent results from the optimized airfoil. This trend is consistent with the TKE distributions of the two airfoils. As shown in Fig. 18, both minimum fuel and baseline airfoils exhibit similar TKE and velocity profiles within their boundary layers, where both analyses are performed at $M = 0.15$, consequently yielding comparable OASPLs.



(a) Boundary layer thickness of the suction side

(b) Boundary layer thickness of the pressure side

Figure 18: Boundary layer characteristics of the minimum fuel airfoil compared with baseline airfoil, conducted at a low Mach condition.

The TEN estimations for baseline and optimized airfoil are done based on the noise prediction model described in Section 4.3. For the same C_L constraint, the resultant α is larger for this

optimum airfoil compared to the baseline airfoil, due to the smaller C_L and C_D compared with the baseline performance under the same flight condition. Hence, in real operations, the higher α can lead to a higher noise level; thus, this airfoil shows a higher TEN value than the baseline case.

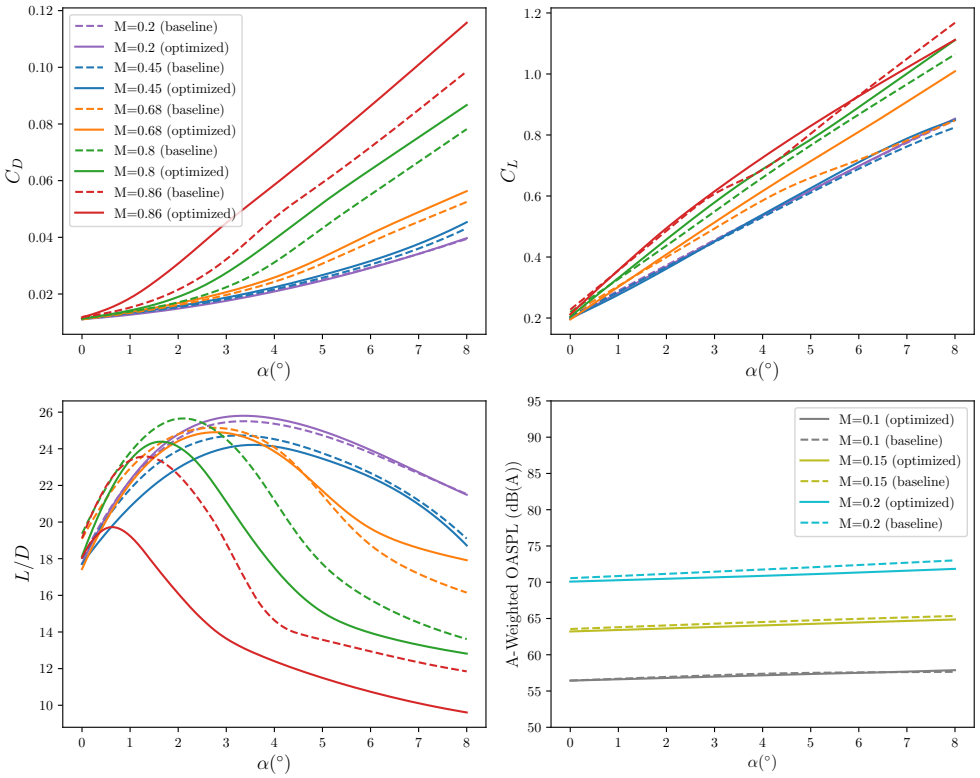


Figure 19: Aerodynamic and aeroacoustic performance comparison between minimax noise airfoil and baseline airfoil for selected representative flight conditions

.

The minimax TEN airfoil, which represents the airfoil in the Pareto front that yields the minimum OASPL, is depicted by the green line in Fig. 15b. The aerodynamic performance of the minimax TEN airfoil is evaluated using surrogate models and presented in Fig. 19. The results show that, except for the low Mach region, the aerodynamic performance of the optimized airfoil is weaker than that of the baseline airfoil under most flight conditions, especially in the transonic region. Compared to the baseline airfoil, the optimized airfoil generates relatively similar C_L but higher C_D, resulting in higher fuel consumption during cruise phases. As such, the potential for fuel reduction would be limited to flight sectors where fuel consumption during the climb phase is more prominent, e.g., in short-haul flights. However, the detailed investigation and comparison between different types of flight missions are beyond the scope of this paper. The bottom-right figure of Fig. 19 presents the aeroacoustic performance of the minimax TEN airfoil, which shows that the optimized airfoil can help reduce TEN under most of the flight conditions in the low Mach region. This observation is consistent with the single-point optimization result, in that this airfoil can reduce TEN in the LTO cycle at the expense of increased fuel consumption. The similarity

with the single-point optimization result was also observed in terms of pressure distribution and boundary layer thickness, indicating similar physical mechanism in the results.

To demonstrate an optimal design that can simultaneously optimize total fuel consumption and TEN, an optimal point from the Pareto front is selected (indicated by the purple line in Fig. 15b). The aft section of this airfoil shows a slight bump on the upper surface, which tends to increase the maximum thickness and change the position of the maximum thickness as compared to the baseline airfoil. For this airfoil, most of C_L and C_D are greater, and the L/D ratio is also higher, though not as high as the L/D increase obtained by using the minimum fuel consumption airfoil. A notable fuel reduction is observed in the test flight. The high L/D in the low Mach region can also contribute to reducing α while maintaining the same level of C_L. Therefore, although the TEN is slightly higher than that of the baseline airfoil under the same flight condition, the smaller α helps mitigate the OASPL.

5.3 Benefits of performing mission-based optimization

The results presented above show that there is a clear tradeoff between the aeroacoustic performance in the low Mach region and the aerodynamic performance in the transonic region. The optimum airfoils obtained from the single-point multi-objective optimization approach may effectively reduce TEN at the low Mach flight condition at which the optimization is performed, but at the expense of higher fuel consumption (up to 11.108%) compared to the baseline airfoil. Although the minimax TEN airfoil can reduce the sound pressure level in the low Mach region, the L/D ratio is markedly lower than the baseline performance under the transonic flow condition. The minimum fuel consumption airfoil shows a satisfactory aerodynamic performance in the cruise phase, but the aeroacoustic properties can only maintain the same level as the baseline case. This tradeoff highlights the importance of considering the entire mission to avoid suboptimal designs in a multi-objective optimization setting, especially when each objective has different dominant flight condition regimes.

In contrast, most of the optimum airfoils from the mission-based optimization approach could simultaneously reduce both metrics. Notably, the fuel consumption can be reduced by up to 9.543%. Despite exhibiting weak aeroacoustic performances in the low Mach region, the maximum TEN during the LTO cycle can still be reduced. The aeroacoustic improvements purely come from the enhanced aerodynamic properties throughout the mission. In addition, the total fuel reduction can also reduce the takeoff weight, which can further alleviate the lift constraint when performing the same mission as the baseline case. These findings reveal the tight coupling of aerodynamics, aeroacoustics, and mission, where a slight change in one aspect can impact the entire situation. This underscores that considerations of aeroacoustic performance and the full range of flight mission cannot be an "afterthought"; they must be considered earlier in the design process to minimize their impacts on each other.

6 Conclusion

This paper presented a mission-based aerodynamic shape optimization framework to investigate the tradeoffs between fuel consumption and TEN, while taking flight operational spectrum into account. The key component of this framework is a detailed flight performance analysis platform, which enables a simultaneous assessment of TEN under realistic flight operating conditions and fuel consumption, where both were considered as the objective functions in a multi-objective ASO. To balance accuracy and efficiency, a three-component TEN model was utilized, consisting of a near-field flow simulation, a semi-empirical wall-pressure fluctuation spectrum model, and an acoustic propagation model. Surrogate models, which estimate the aerodynamic coefficients and acoustic sound pressure level, were also built to reduce the overall computational costs. Furthermore, a POD-based CST method was used to represent airfoil geometry variations efficiently. To define a suitable, realistic design space for surrogate model construction purposes, flight-condition distributions extracted from actual flight missions were used as reference.

In addition to running a conventional single-point optimization, a newly developed mission-based multi-objective ASO formulation was demonstrated in this paper. The objectives were to minimize total fuel consumption and maximum TEN during the LTO cycle. To use the same metrics in the comparison between single-point and mission-based results, the fuel performance of the optimal airfoils—upon converting the 2D aerodynamic coefficient values to the corresponding 3D values to represent aircraft wings—was evaluated for the nominal flight mission. The results revealed that the single-point optima reduced the maximum TEN at the expense of increased total fuel consumption. This is due to the tradeoff between the aeroacoustic performance in the low Mach region—which constitutes the flight condition considered in the single-point optimization—and the aerodynamic performance in the transonic region—which determines the fuel consumption. While this tendency still appeared in the mission-based results, the resulting optimum airfoils could still reduce the two metrics simultaneously, albeit the tradeoff, thanks to the enhanced overall aerodynamic performance. Our results and observations highlighted the importance of incorporating the aeroacoustic and mission aspects into ASO formulations, where the latter was needed to consider a wider spectrum of flight conditions in the design and optimization process.

Indeed, considering only TEN as a noise metric is still insufficient to model aircraft noise comprehensively. Nonetheless, including a noise metric that is a direct consequence of airfoil shape takes airfoil design optimization one step further, in addition to providing insight into the tradeoff between aerodynamic and aeroacoustic performance—which are the main objectives of this work. We also acknowledge that the resulting optimized aerodynamic shape designs presented in this paper—which mostly pertain to 2D airfoil designs—still have limited implications on realistic wing designs that can reduce fuel consumption and noise. At present, the combined complexities from aerodynamics, aeroacoustics, and flight mission analyses limit the computations to 2D designs. Note, however, that their conversion to "pseudo" 3D performance values has been performed and validated for more realistic analyses. Despite these limitations, we believe that our optimization results still provide useful insights into the interplay between aerodynamics, aeroacoustics, and flight

operational variations, which would provide a strong basis and motivation for further optimization studies involving 3D wing models. The mission-based optimization is key in the tradeoff study, as it can evaluate the aerodynamic and TEN performances under different realistic flight conditions, which cannot be achieved by a conventional single-point optimization. To the best of our knowledge, we have not seen such considerations and results in prior studies. While some prior works on multi-objective aerodynamic-aeroacoustic optimization of airfoils have been published [11, 44, 34], they did not consider flight operational variations, further highlighting the importance and relevance of mission-based optimization.

Furthermore, the modular nature of the developed methodology would make replacing the current models with other higher-fidelity models (such as a coupled CFD and computational aeroacoustic model using a permeable surface Ffowcs Williams-Hawkings approach that can predict the far-field noise of the 3D wing), once available, more practicable. In the future, this framework can be further extended to perform more detailed shape optimizations (especially for 3D wings) and tradeoff studies involving more comprehensive aerodynamic and aeroacoustic metrics, for both conventional and unconventional configurations.

Acknowledgements

This work was supported by the Hong Kong Research Grants Council Early Career Scheme (Project No. 26202116) and Research Support from Chau Hoi Shuen Foundation (Project No. R9052). The computational fluid dynamics simulations were performed on the Tianhe-2 supercomputing platform. The authors would like to thank Cathay Pacific Airways Limited for providing the data used in this study under the Data Partnership Agreement between the airline and the Department of Mechanical and Aerospace Engineering, HKUST. The authors additionally thank the anonymous reviewers of this paper for their helpful suggestions.

References

[1] ICAO Secretariat, Climate Change Mitigation: CORSIA (2021).

[2] S. Le Clainche, E. Ferrer, S. Gibson, E. Cross, A. Parente, R. Vinuesa, Improving aircraft performance using machine learning: A review, Aerospace Science and Technology 138 (2023) 108354. doi:10.1016/j.ast.2023.108354.

[3] M. Pacull, Transport aircraft noise reduction technologies (A340-300), in: Proceedings of the International Symposium: Which Technologies for Future Aircraft Noise Reduction, Arcachon, France, 2002.

[4] N. E. Antoine, I. M. Kroo, Aircraft Optimization for Minimal Environmental Impact, Journal of Aircraft 41 (4) (2004) 790–797. doi:10.2514/1.71.

[5] A. Jameson, Aerodynamic design via control theory, Journal of scientific computing 3 (1988) 233–260. doi:10.1007/BF01061285.

[6] T. Göçmen, B. Özerdem, Airfoil optimization for noise emission problem and aerodynamic performance criterion on small scale wind turbines, Energy 46 (1) (2012) 62–71, Energy and Exergy Modelling of Advance Energy Systems. doi:10.1016/j.energy.2012.05.036.

[7] D. Casalino, F. Diozzi, R. Sannino, A. Paonessa, Aircraft noise reduction technologies: A bibliographic review, Aerospace Science and Technology 12 (1) (2008) 1–17. doi:10.1016/j.ast.2007.10.004.

[8] F. Collier, NASA Aeronautics Environmentally Responsible Aviation Project—Real Solutions for Environmental Challenges Facing Aviation, in: 50th AIAA Aerospace Sciences Meeting and Exhibit, no. NF1676L-14056, 2012.

[9] European Commission and Directorate-General for Mobility and Transport and Directorate-General for Research and Innovation, Flightpath 2050 – Europe's vision for aviation – Maintaining global leadership and serving society's needs, Publications Office, 2011. doi:10.2777/50266.

[10] S. Hosder, J. Schetz, B. Grossman, W. Mason, Airframe Noise Modeling Appropriate for Multidisciplinary Design and Optimization, in: 42nd AIAA Aerospace Sciences Meeting and Exhibit, 2004, p. 698. doi:10.2514/6.2004-698.

[11] B. Y. Zhou, T. A. Albring, N. R. Gauger, T. D. Economon, F. Palacios, J. J. Alonso, A Discrete Adjoint Framework for Unsteady Aerodynamic and Aeroacoustic Optimization, in: 16th AIAA/ISSMO Multidisciplinary Analysis and Optimization Conference, 2015, p. 3355. doi:10.2514/6.2015-3355.

[12] J. Jouhaud, P. Sagaut, M. Montagnac, J. Laurenceau, A surrogate-model based multidisciplinary shape optimization method with application to a 2D subsonic airfoil, Computers & Fluids 36 (3) (2007) 520–529. doi:10.1016/j.compfluid.2006.04.001.

[13] S. E. Cliff, J. J. Reuther, D. A. Saunders, R. M. Hicks, Single-Point and Multipoint Aerodynamic Shape Optimization of High-Speed Civil Transport, Journal of Aircraft 38 (6) (2001) 997–1005. doi:10.2514/2.2886.

[14] J. J. Reuther, A. Jameson, J. J. Alonso, M. J. Rimlinger, D. Saunders, Constrained Multipoint Aerodynamic Shape Optimization Using an Adjoint Formulation and Parallel Computers, Part 1, Journal of Aircraft 36 (1) (1999) 51–60. doi:10.2514/2.2413.

[15] J. T. Hwang, J. P. Jasa, J. R. R. A. Martins, High-Fidelity Design-Allocation Optimization of a Commercial Aircraft Maximizing Airline Profit, Journal of Aircraft 56 (3) (2019) 1164–1178. doi:10.2514/1.C035082.

[16] R. P. Liem, J. R. Martins, G. K. Kenway, Expected drag minimization for aerodynamic design optimization based on aircraft operational data, Aerospace Science and Technology 63 (2017) 344 – 362. doi:10.1016/j.ast.2017.01.006.

[17] X. Chai, X. Yu, Y. Wang, Multipoint optimization on fuel efficiency in conceptual design of wide-body aircraft, Chinese Journal of Aeronautics 31 (1) (2018) 99–106. doi:10.1016/j.cja.2017.10.006.

[18] J. Li, J. Cai, Massively Multipoint Aerodynamic Shape Design via Surrogate-Assisted Gradient-Based Optimization, AIAA Journal 58 (5) (2020) 1949–1963. doi:10.2514/1.J058491.

[19] Y. Cai, D. Rajaram, D. N. Mavris, Multi-mission Multi-objective Optimization in Commercial Aircraft Conceptual Design, in: AIAA Aviation 2019 Forum, 2019, p. 3577. doi:10.2514/6.2019-3577.

[20] J. P. Jasa, J. T. Hwang, J. R. Martins, Open-source coupled aerostructural optimization using Python, Structural and Multidisciplinary Optimization 57 (4) (2018) 1815–1827. doi:10.1016/j.cja.2017.10.006.

[21] E. Adler, J. R. Martins, Aerostructural wing design optimization considering full mission analysis, in: AIAA SCITECH 2022 Forum, 2022, p. 0382. doi:10.2514/6.2022-0382.

[22] Y. C. Küçükosman, J. Christophe, C. Schram, Trailing edge noise prediction based on wall pressure spectrum models for NACA0012 airfoil, Journal of Wind Engineering and Industrial Aerodynamics 175 (2018) 305–316. doi:10.1016/j.jweia.2018.01.030.

[23] T. F. Brooks, D. S. Pope, M. A. Marcolini, Airfoil self-noise and prediction, Tech. rep., NASA (1989).

[24] G. Romani, E. Grande, F. Avallone, D. Ragni, D. Casalino, Performance and noise prediction of low-Reynolds number propellers using the Lattice-Boltzmann method, Aerospace Science and Technology 125 (2022) 107086. doi:10.1016/j.ast.2021.107086.

[25] I. Solís-Gallego, A. Meana-Fernández, J. Fernández Oro, K. Argüelles Díaz, S. Velarde-Suárez, LES-based numerical prediction of the trailing edge noise in a small wind turbine airfoil at different angles of attack, Renewable Energy 120 (2018) 241–254. doi:10.1016/j.renene.2017.12.082.

[26] M. Herr, R. Ewert, C. Rautmann, M. Kamruzzaman, D. Bekiropoulos, R. Arina, A. Iob, P. Batten, S. Chakravarthy, F. Bertagnolio, Broadband Trailing-Edge Noise Predictions—Overview of BANC-III Results, in: 21st AIAA/CEAS Aeroacoustics Conference, 2015, p. 2847. doi:10.2514/6.2015-2847.

[27] C. Doolan, C. Albarracin Gonzalez, C. Hansen, Statistical estimation of turbulent trailing edge noise, in: Proceedings of 20th International Congress on Acoustics, American Institute of Aeronautics and Astronautics, 2010.

[28] R. K. Amiet, Acoustic radiation from an airfoil in a turbulent stream, Journal of Sound and Vibration 41 (4) (1975) 407–420. doi:10.1016/S0022-460X(75)80105-2.

[29] M. S. Howe, Acoustics of fluid-structure interactions, Cambridge university press, 1998.

[30] W. K. Blake, Mechanics of flow-induced sound and vibration, Volume 2: Complex flow-structure interactions, Academic Press, 2017.

[31] S. Lee, Empirical Wall-Pressure Spectral Modeling for Zero and Adverse Pressure Gradient Flows, AIAA Journal 56 (5) (2018) 1818–1829. doi:10.2514/1.J056528.

[32] R. P. Liem, G. K. W. Kenway, J. R. R. A. Martins, Multimission Aircraft Fuel Burn Minimization via Multipoint Aerostructural Optimization, AIAA Journal 53 (1) (2015) 104–122. doi:10.2514/1.J052940.

[33] Z. Lyu, G. K. Kenway, J. R. R. A. Martins, Aerodynamic shape optimization studies on the Common Research Model wing benchmark, AIAA Journal 53 (4) (2015) 968–985. doi:10.2514/1.J053318.

[34] B. Y. Zhou, T. Albring, N. R. Gauger, C. R. da Silva, T. D. Economon, J. J. Alonso, Efficient Airframe Noise Reduction Framework via Adjoint-Based Shape Optimization, AIAA Journal 59 (2) (2021) 580–595. doi:10.2514/1.J058917.

[35] A. B. Lambe, J. R. Martins, Extensions to the design structure matrix for the description of multidisciplinary design, analysis, and optimization processes, Structural and Multidisciplinary Optimization 46 (2) (2012) 273–284. doi:10.1007/s00158-012-0763-y.

[36] Y. Lyu, R. P. Liem, Flight performance analysis with data-driven mission parameterization: mapping flight operational data to aircraft performance analysis, Transportation Engineering 2 (2020) 100035. doi:10.1016/j.treng.2020.100035.

[37] X. Zhang, Aircraft noise and its nearfield propagation computations, Acta Mechanica Sinica 28 (4) (2012) 960–977. doi:10.1007/s10409-012-0136-1.

[38] C. Rautmann, Numerical Simulation Concept for Low-Noise Wind Turbine Rotors, Ph.D. thesis, AS-BS (2017).

[39] F. R. Menter, Two-equation eddy-viscosity turbulence models for engineering applications, AIAA Journal 32 (8) (1994) 1598–1605. doi:10.2514/3.12149.

[40] M. A. Bouhlel, J. T. Hwang, N. Bartoli, R. Lafage, J. Morlier, J. R. Martins, A Python surrogate modeling framework with derivatives, Advances in Engineering Software 135 (2019) 102662. doi:10.1016/j.advengsoft.2019.03.005.

[41] Lissys Ltd, Piano-x, https://www.lissys.uk/PianoX.html, accessed: 2022-04-05 (2008).

[42] M. Kamruzzaman, D. Bekiropoulos, T. Lutz, W. Würz, E. Krämer, A Semi-Empirical Surface Pressure Spectrum Model for Airfoil Trailing-Edge Noise Prediction, International Journal of Aeroacoustics 14 (5-6) (2015) 833–882. doi:10.1260/1475-472X.14.5-6.833.

[43] J. F. Nash, Turbulent-Boundary-Layer Behaviour and the Auxiliary Equation, Tech. rep., MINISTRY OF AVIATION AERONAUTICAl RESEARCH COUNCIL (1966).

[44] N. Ricks, P. Tsirikoglou, F. Contino, G. Ghorbaniasl, A CFD-based methodology for aerodynamic-aeroacoustic shape optimization of airfoils, in: AIAA Scitech 2020 Forum, 2020, p. 1729. doi:10.2514/6.2020-1729.

[45] M. R. Catlett, J. M. Anderson, J. B. Forest, D. O. Stewart, Empirical Modeling of Pressure Spectra in Adverse Pressure Gradient Turbulent Boundary Layers, AIAA Journal 54 (2) (2016) 569–587. doi:10.2514/1.J054375.

[46] B. M. Kulfan, J. Bussoletti, "Fundamental" Parameteric Geometry Representations for Aircraft Component Shapes, in: 11th AIAA/ISSMO Multidisciplinary Analysis and Optimization Conference, 2006, p. 6948. doi:10.2514/6.2006-6948.

[47] D. A. Masters, N. J. Taylor, T. Rendall, C. B. Allen, D. J. Poole, Review of Aerofoil Parameterisation Methods for Aerodynamic Shape Optimisation, in: 53rd AIAA Aerospace Sciences Meeting, 2015, p. 0761. doi:10.2514/6.2015-0761.

[48] X. Wu, W. Zhang, X. Peng, Z. Wang, Benchmark aerodynamic shape optimization with the POD-based CST airfoil parametric method, Aerospace Science and Technology 84 (2019) 632–640. doi:10.1016/j.ast.2018.08.005.

[49] T. Long, Y. Wu, Z. Wang, Y. Tang, D. Wu, Y. Yu, Efficient aero-structure coupled wing optimization using decomposition and adaptive metamodeling techniques, Aerospace Science and Technology 95 (2019) 105496. doi:10.1016/j.ast.2019.105496.

[50] M. D. McKay, W. J. Conover, R. J. Beckman, A Comparison of Three Methods for Selecting Values of Input Variables in the Analysis of Output from a Computer Code, Technometrics 21 (2) (1979) 239–245.

[51] V. Aute, K. Saleh, O. Abdelaziz, S. Azarm, R. Radermacher, Cross-validation based single response adaptive design of experiments for kriging metamodeling of deterministic computer simulations, Structural and Multidisciplinary Optimization 48 (3) (2013) 581–605. doi:10.1007/s00158-013-0918-5.

[52] N. Cressie, The Origins of Kriging, Mathematical Geology 22 (3) (1990) 239–253.

[53] J. Yanto, R. P. Liem, Aircraft fuel burn performance study: A data-enhanced modeling approach, Transportation Research Part D: Transport and Environment 65 (2018) 574–595. doi:10.1016/j.trd.2018.09.014.

[54] S. Glegg, W. Devenport, Aeroacoustics of low Mach number flows: fundamentals, analysis, and measurement, Academic Press, 2017.